The SAMI Galaxy Survey: the role of disc fading and progenitor bias in kinematic transitions

S. M. Croom [1,2,3]★ D. S. Taranu,[3,4,5] J. van de Sande [1,2] C. D. P. Lagos,[2,4] K. E. Harborne,[2,4]
J. Bland-Hawthorn [1,2] S. Brough [6,2] J. J. Bryant,[1,2] L. Cortese [2,4] C. Foster [1,2] M. Goodwin,[7]
B. Groves,[2,4,8] A. Khalid [1] J. Lawrence,[7] A. M. Medling [9] S. N. Richards,[10] M. S. Owers [11,12]
N. Scott [1,2] and S. P. Vaughan [1,2]

[1]*Sydney Institute for Astronomy, School of Physics, University of Sydney, Sydney, NSW 2006, Australia*
[2]*ASTRO3D: ARC Centre of Excellence for All-sky Astrophysics in 3D, Canberra, ACT 2601, Australia*
[3]*CAASTRO: ARC Centre of Excellence for All-sky Astrophysics, Canberra, ACT 2601, Australia*
[4]*International Centre for Radio Astronomy Research, University of Western Australia, 35 Stirling Highway, Crawley, WA 6009, Australia*
[5]*Department of Astrophysical Sciences, Princeton University, 4 Ivy Lane, Princeton, NJ 08544, USA*
[6]*School of Physics, University of New South Wales, Sydney, NSW 2052, Australia*
[7]*Australian Astronomical Optics – Macquarie, 105 Delhi Rd, North Ryde, NSW 2113, Australia*
[8]*Research School of Astronomy and Astrophysics, Australian National University, Mt Stromlo Observatory, Cotter Rd, Weston Creek, ACT 2611, Australia*
[9]*Ritter Astrophysical Research Center University of Toledo, Toledo, OH 43606, USA*
[10]*SOFIA Science Center, USRA, NASA Ames Research Center, Building N232, M/S 232-12, PO Box 1, Moffett Field, CA 94035-0001, USA*
[11]*Department of Physics and Astronomy, Macquarie University, Sydney, NSW 2109, Australia*
[12]*Astronomy, Astrophysics and Astrophotonics Research Centre, Macquarie University, Sydney, NSW 2109, Australia*

ABSTRACT
We use comparisons between the Sydney-AAO Multi-object Integral Field Spectrograph (SAMI) Galaxy Survey and equilibrium galaxy models to infer the importance of disc fading in the transition of spirals into lenticular (S0) galaxies. The local S0 population has both higher photometric concentration and lower stellar spin than spiral galaxies of comparable mass and we test whether this separation can be accounted for by passive aging alone. We construct a suite of dynamically self-consistent galaxy models, with a bulge, disc, and halo using the GALACTICS code. The dispersion-dominated bulge is given a uniformly old stellar population, while the disc is given a current star formation rate putting it on the main sequence, followed by sudden instantaneous quenching. We then generate mock observables (*r*-band images, stellar velocity, and dispersion maps) as a function of time since quenching for a range of bulge/total (*B*/*T*) mass ratios. The disc fading leads to a decline in measured spin as the bulge contribution becomes more dominant, and also leads to increased concentration. However, the quantitative changes observed after 5 Gyr of disc fading cannot account for all of the observed difference. We see similar results if we instead subdivide our SAMI Galaxy Survey sample by star formation (relative to the main sequence). We use EAGLE simulations to also take into account progenitor bias, using size evolution to infer quenching time. The EAGLE simulations suggest that the progenitors of current passive galaxies typically have slightly higher spin than present day star-forming disc galaxies of the same mass. As a result, progenitor bias moves the data further from the disc fading model scenario, implying that intrinsic dynamical evolution must be important in the transition from star-forming discs to passive discs.

Key words: galaxies: evolution – galaxies: kinematics and dynamics – galaxies: structure.

1 INTRODUCTION

Revealing the underlying physical processes driving the transformation of galaxies remains one of the central aims of astrophysics. We know that through cosmic time the galaxy population tends to transition from star-forming to passive, from blue to red, and from morphologically late type (e.g. spirals) to early type (e.g. S0s). These transitions are undoubtedly related to each other; for example, colour

is to first order related to mean stellar age, and so directly tied to the star formation history of a galaxy. The connection between star formation history and morphology is also significant, with most star-forming galaxies being late types, and most passive galaxies being early types. However, this is not exactly a one-to-one relation, as several works have shown (e.g. Schawinski et al. 2009; Masters et al. 2010; Davies et al. 2019)

Environment must play a significant role in these transformations, given the well known morphology–density (e.g. Dressler 1980) and star formation rate (SFR)–density relations (e.g. Lewis et al. 2002). This is particularly so for the expected transformation from

★ E-mail: scott.croom@sydney.edu.au

spiral to lenticular (or S0) galaxies. The fraction of S0s grows monotonically as environment becomes richer, at the expense of spirals. Despite environment being clearly implicated in the spiral–S0 transformation, this has not brought us directly to the physical cause of the transformation, as there remains a number of plausible mechanisms that could play a part. In fact, it is likely that many of the proposed mechanisms have a role, but that their importance changes as a function of environment.

Measurements as a function of redshift show that as we go back in time the S0 fraction declines in dense environments. This decline happens both in clusters (Dressler et al. 1997) and groups (Just et al. 2010). In fact, the change in S0 fraction with cosmic time appears stronger in groups (defined as having dispersion $\sigma < 750\,\mathrm{km\,s^{-1}}$ by Just et al.) than clusters ($\sigma > 750\,\mathrm{km\,s^{-1}}$). Similar evolution is seen in the colour (e.g. Butcher & Oemler 1984) and SFRs (e.g. Elbaz et al. 2007) of galaxies in high-density environments.

Arguably the simplest process that converts a spiral to an S0 is so-called strangulation (e.g. Larson, Tinsley & Caldwell 1980), where continued inflow of gas on to the disc is inhibited by the galaxy's environment. The star formation in the disc slowly shuts down as remaining fuel is consumed. More violent interactions, such as ram pressure stripping (Gunn & Gott 1972) can remove gas directly from the disc. Ram pressure may be expected to act quickly, but as a galaxy falls into an overdense region, the increase in ram pressure can be gradual, leading to slower transitions (Roediger & Brüggen 2007). Other physical effects can also play a role. Thermal conduction from the hot intra-cluster medium to the cooler interstellar medium of a galaxy can potentially lead to much faster gas loss (Vijayaraghavan & Sarazin 2017a). However, simulations including magnetic fields find that thermal conduction is suppressed as the hot electrons have to follow the magnetic field lines (Vijayaraghavan & Sarazin 2017b). Comparisons between hydrodynamic simulations of gas stripping with and without magnetic fields by Ramos-Martínez, Gómez & Pérez-Villegas (2018) find that gas removal is less efficient, and happens at larger radius, when magnetic fields are present. Another contributing factor is turbulent viscosity that could enhance stripping (Nulsen 1982), although hydrodynamical simulations seem to suggest that viscosity does not severely alter the gas mass lost from discs (Roediger & Brüggen 2008).

As well as the primarily gas-physics related processes, gravitational interactions with the other galaxies or the group/cluster potential could also be important for the transition from spiral to S0. Simulations suggest that some galaxy–galaxy mergers can lead to S0-like morphology. These include minor mergers (Bekki 1998) and at least a fraction of major mergers with favourable impact parameters and progenitor spins (Querejeta et al. 2015). Less severe dynamical interactions can also play a role. Bekki & Couch (2011, henceforth BC11) show that repeated tidal interactions with other galaxies within a group environment have the effect of heating the stellar disc, and triggering nuclear star formation to build a bulge.

Many observations of S0 galaxies have been used to try and ascertain which processes are most important. S0 galaxies are found to follow a well-defined Tully–Fisher (TF) relation (Mathieu, Merrifield & Kuijken 2002; Rawle et al. 2013) with an offset from the same relation for spirals. The offset is largely consistent with S0s having older stellar populations. However, Williams, Bureau & Cappellari (2010) finds that there remains a small offset between the spiral and S0 TF relation even when stellar mass or dynamical mass is used. This offset may mean that galaxies undergo a small amount of contraction as they transition from S0 to spiral. An alternative to contraction may be evolution in the zero-point of the spiral TF, although recent work carefully comparing high- and low-redshift gas

kinematics suggests little evolution of the TF relation (Tiley et al. 2019). The S0 TF relation therefore seems broadly consistent with gas related quenching followed by the fading of the disc, although Tapia et al. (2017) argue that a similar TF relation could be derived through merging.

Decomposing S0 galaxies into a bulge and disc provides a different view. Christlein & Zabludoff (2004) suggest that S0 bulges are more luminous than can be explained by simple disc fading, but this disagrees with a combination of decomposition and colour analysis (Head et al. 2014) that is used to argue for disc fading. Kinematic decomposition allows us to go one step further, and Cortesi et al. (2013) derive the TF and Faber–Jackson relations for S0 discs and bulges separately. Their small sample shows consistent offsets of S0s in both dynamical scaling relations, that again points to more than just disc fading for the formation of S0s. In contrast, Oh et al. (2020) have recently examined the kinematics of decomposed bulges and discs from the Sydney-AAO Multi-object Integral Field Spectrograph (SAMI) Galaxy Survey across a wide range in mass and morphology. They find that the discs for both early- and late-type galaxies sit on the same stellar-mass TF relation.

Measuring the stellar population ages and metallicities of Virgo cluster S0 bulges and discs separately, Johnston, Aragón-Salamanca & Merrifield (2014) find that bulges have younger ages. This points to the last star formation in S0s being centrally concentrated, although it could still be occurring in the inner disc, rather than within a dispersion-supported bulge. The Johnston et al. (2014) measurement is consistent with the observation that star formation is typically more centrally concentrated in high-density environments, both in clusters (Koopmann & Kenney 2004) and groups (Schaefer et al. 2017, 2019). The younger central ages could be due to star formation enhanced by gas inflows toward the central parts of the galaxies, caused by dynamical interactions. Alternatively, ram pressure may only remove the outer gas reservoir, allowing central star formation to continue for some time (Cen 2014).

The advent of large-scale integral field spectroscopy surveys (e.g. Croom et al. 2012; Bundy et al. 2015; Sánchez et al. 2016) has opened up another window on to the question of S0 formation. They allow estimates of the fraction of dynamical support provided by rotational velocity (V) and random orbits (dispersion, σ). These can be combined into the spin parameter proxy, $\lambda_R = \langle R|V|\rangle / \langle R\sqrt{V^2 + \sigma^2}\rangle$ (Emsellem et al. 2011), where the radius R is typically taken as the effective radius, R_e. Querejeta et al. (2015) use the Calar Alto Legacy Integral Field spectroscopy Area survey (CALIFA) to argue that the transformation of spirals to S0s cannot simply be disc fading, as S0s have both lower λ_R and higher concentration (defined as the ratio of the radii containing 90 and 50 per cent of total galaxy flux, $c = R_{90}/R_{50}$). Instead, they propose that merging is able to translate galaxies in both λ_R and concentration. A similar conclusion is drawn using galaxies observed with the SAMI by Fogarty et al. (2015) based on cluster galaxies. However, in this case, the authors argue that the trend in λ_R and concentration is consistent with repeated dynamical encounters (BC11).

The λ_R versus concentration plane seems to provide a useful tool for diagnosing the nature of transformations, but care has to be taken over interpretation. Both measurements are light weighted, and so can be influenced by radial differences in stellar populations. Carollo et al. (2016) show that while quenched galaxies have higher bulge/total (B/T) flux ratios than star-forming disc galaxies, their bulges are not more luminous. Rather, their discs have lower luminosity. The lower disc luminosity is a natural consequence of the disc fading as star formation ceases. Given the bulge and disc have different light profiles (the bulge typically with higher Sérsic

index, n), a reduced light contribution from the disc can lead to higher measured concentration, without any underlying structural change. Likewise, λ_R measurements are flux weighted, so fading of a disc can lead to the bulge component dominating the measured dynamics. If the bulge is dispersion dominated (or at least has less rotational support than the disc), then λ_R can be reduced, again without any underlying structural change in the galaxy.

The aim of this paper is to assess how large the impact of disc fading is on λ_R and concentration. In particular, we wish to know whether differences between the spiral and S0 populations seen in this parameter space can be explained solely by disc fading, or if other physical effects are also required. To do this we build self-consistent dynamical models using the GALACTICS code (Kuijken & Dubinski 1995; Widrow, Pym & Dubinski 2008), and from them generate synthetic images and velocity fields using the MAGRITE code developed by Taranu et al. (2017). This approach allows us to control the stellar population age of the separate dynamical components (bulge and disc). We then compare the results of our models to integral field data from the SAMI Galaxy Survey (Croom et al. 2012; Bryant et al. 2015).

A challenge in comparing spirals and S0s is that we are usually making the comparison at the same redshift, while the progenitors of today's S0s were spirals at an earlier epoch. Measurements of high redshift gas kinematics appear to show much greater turbulence in discs (e.g. Wisnioski et al. 2015) at early times, and this could translate to higher stellar disc dispersion. Recent simulations similarly show increased dispersion at high redshift (Pillepich et al. 2019). To take this into account we will use EAGLE simulations (Schaye et al. 2015) to make estimates of this progenitor bias. Comparisons of star formation and kinematics using SAMI and EAGLE have already been used to highlight the importance of progenitor bias by Cortese et al. (2019). They find that little evidence of structural change when satellite galaxies are quenched.

In Section 2, we describe the details of our model, including our assumed star formation histories. In Section 3, we present the result of making λ_R and concentration measurements on the simulations. Section 4 contains a comparison of our models with measurements from the SAMI Galaxy Survey, as well as the discussion of the role of progenitor bias. We give concluding remarks in Section 5. Throughout this paper, we assume a cosmology with $\Omega_m = 0.3$, $\Omega_\Lambda = 0.7$, and $H_0 = 70 \, \text{km s}^{-1}\text{Mpc}^{-1}$.

2 DISC FADING MODELS

Our main goal is to test whether disc fading is consistent with the difference between spirals and S0s in the λ_R–concentration plane. To do this, we need simulated galaxies that have realistic dynamics and morphological structure. We also need to apply different star formation histories to the bulge and disc components. Importantly, the derived kinematics need to be light weighted, so that we can fully capture the effects of only varying the M/L of the stellar populations without modifying their underlying distribution functions. The methodology presented by Taranu et al. (2017) to model SAMI data fulfils all of these criteria and we will now describe its key features.

2.1 Equilibrium galaxy models

The equilibrium galaxy models are built using a modified version of the GALACTICS code (Kuijken & Dubinski 1995; Widrow et al. 2008), detailed in appendix F of Taranu et al. (2017). GALACTICS computes equilibrium phase-space distribution functions for three components:

an exponential stellar disc with a sech^2 vertical density profile; a flattened, non-rotating Sérsic (1963) profile stellar bulge; and a slightly flattened halo with a generalized (Navarro, Frenk & White 1997, hereafter NFW) profile. Typically, the equilibrium solution is close to the original parameters, but with the spherical components (bulge and halo) flattened by the presence of the disc.

There is a large amount of flexibility with the GALACTICS approach. However, we choose a restricted range of parameters, relevant to demonstrating the impact of disc fading. The NFW halo density profile is

$$\rho \propto \frac{1}{(r/r_h)^\alpha (1 + r/r_h)^{(\beta - \alpha)}}, \tag{1}$$

where we choose $\alpha = 1$, $\beta = 2.3$, and $r_h = 6.07 \, \text{kpc}$. The halo is nearly spherical (mildly vertically flattened by the disc), non-rotating and truncated beyond 300 kpc. Modification of the halo parameters has little impact on the stellar components beyond the expected change in the rotation curve. The bulge is also nearly spherical and non-rotating, although it can be somewhat flattened as it responds to the potential of a massive disc. We could choose models with a rotating bulge, but a non-rotating bulge leads to the largest difference in kinematics with disc fading, so provides a robust upper limit on the role of disc fading. The bulge follows a 'classical' de Vaucouleurs (1948) profile (Sérsic $n_s = 4.0$), although changes to the value of n_s have modest impacts on our results compared to changes in the bulge scale-length. In order to generate physically realistic galaxies, we use the measured stellar mass versus R_e relations from Lange et al. (2016). They fit relations of the form

$$R_e = a \left(\frac{M_*}{10^{10} \, \text{M}_\odot} \right)^b \tag{2}$$

to bulge and disc properties measured from r-band SDSS imaging. For bulges, we use values of $a = 1.667 \, \text{kpc}$ and $b = 0.477$ to approximate the separate low- and high-mass power-law relations. For discs, we use $a = 5.0 \, \text{kpc}$ and $b = 0.301$, which is slightly steeper than Lange et al. (2016) to account for the difficulty of accurately measuring the size of very small discs. The disc density profile is

$$\rho \propto \exp(R/R_d)\text{sech}^2(z/z_d). \tag{3}$$

Here R is the cylindrical radius in the disc and z is the vertical distance off the disc. We choose the disc scale-length, R_d, which is equivalent to an R_e defined using the above relations from Lange et al. (2016). We assume a scale height of $z_d = 0.75 \, \text{kpc}$. The structural parameter that most influences our results is the ratio of bulge and disc scale-lengths. Changes of scale-length can have important consequences for our measurements. For example, a larger disc scale-length, together with a smaller bulge, would lead to large changes in R_e as the disc fades and the bulge becomes more important. These changes can in turn have a significant effect on the measured λ_R. For this reason, we have chosen to use the observed relations of Lange et al. (2016) for our models.

The simulated galaxies are built by sampling the underlying distribution functions, so their spatial resolution is largely set by this discrete sampling. The bins for sampling are adaptive. Averaged over all bins the resolution is $\sim 150 \, \text{pc}$, but, in practice, it is better than 100 pc in all but the outer disc. This is an order of magnitude better than the observational resolution.

We generate a range of models with bulge/total mass fraction (B/T) of 0.0 to 1.0 in steps of 0.1. In each case, the total stellar mass of the combined bulge and disc is $10^{10.8} \, \text{M}_\odot$.

2.2 Generating synthetic images and kinematics

There are several steps required to simulate observed kinematics from the dynamical models presented above. The early stages make use of the synthetic observation pipeline 'This Is Not A Pipeline' (TINAP; first described by Taranu, Dubinski & Yee 2013) to generate images and kinematic maps, following the methods used to generate synthetic SAMI data described in Taranu et al. (2017).

The first step is to assign a star formation history separately to the bulge and disc. As we are primarily interested in the maximum impact that disc fading can have, we assign a uniformly old age to the bulge for all models. The bulges are assumed to have formed in a single instantaneous burst 10 Gyr ago. The discs begin forming stars 12.9 Gyr in the past with a slow exponentially declining SFR $\propto \exp[-(t-t_0)/\tau]$, using a τ of 5 Gyr. Then we abruptly stop star formation (e.g. disc star formation instantaneously drops to zero) at times varying from 0 to 5 Gyr in the past, in 1-Gyr intervals. We assume solar metallicity for both the bulge and disc. Based on the SFH of each component we derive the M/L in three bands: SDSS g and r, as well as an effective SAMI band over the wavelength range that we typically measure kinematics (that we will call SAMIgr). To calculate M/L, we use the model grids of Maraston & Strömbäck (2011). The stellar populations are assumed to be uniform within each component (i.e. bulge and disc). The dynamical masses of the bulge and disc include the contributions from evolved stars and stellar remnants (the proportion of which also varies with the SFH).

The distribution functions of the bulge and disc are then numerically integrated to create cubes of the observed luminosity density in regular spatial and projected velocity bins. The galaxy is placed at a redshift of 0.04, giving a scale of 0.791 kpc arcsec^{-1} (typical of SAMI galaxies). For each model, we sample a range of inclinations from face-on to edge-on in steps of 15°.

The kinematic measurements of the models are done at the native resolution of the simulations ($\sim$100 pc, equivalent to $\sim$0.13 arcsec, an order of magnitude better than the typical observational measurements). This is because we apply a beam-smearing correction (Harborne et al. 2020a) to the λ_{R_e} measurements that we make on the SAMI data (see Section 4.1 for details). However, we do convolve the simulations with the expected seeing to measure concentration, as this is a seeing convolved quantity. We also examine the impact of seeing on the kinematic measurements (see Section 3.2). To simulate seeing, the cube is convolved with a Moffat (1969) profile PSF,

$$I(r) = I_0[1 + (r/R)^2]^{-\beta_m}, \tag{4}$$

where the full width at half-maximum (FWHM) is given by FWHM= $2R\sqrt{2^{(1/\beta_m)} - 1}$. We use FWHM = 1.8 arcsec and β_m =2.25 (these are typical of SAMI observations and specifically based on the SAMI data of G79635; Taranu et al. 2017). Similarly, the cube is convolved with a Gaussian of FWHM 150 km s^{-1} along the projected velocity axis in order to match the spectral resolution of SAMI's blue arm. The oversampled cube is then rebinned into 0.5 arcsec spaxels and 60 km s^{-1} pixels (similar to the SAMI blue arm sampling). The line-of-sight velocity distribution in each spaxel is fit with a Gaussian to derive the mean velocity and dispersion, with the aforementioned instrumental velocity resolution subtracted in quadrature. It is worth noting that because we derive the luminosity density spatially and in projected velocity the derived kinematics are light weighted (to the above-mentioned SAMIgr band).

The models are also projected into SDSS g- and r-band images, sampled by 0.2-arcsec pixels and convolved with a Moffat PSF of 1.16 and 0.54 arcsec in the g and r bands, respectively. All of these seeing parameters match those used to model a SAMI galaxy
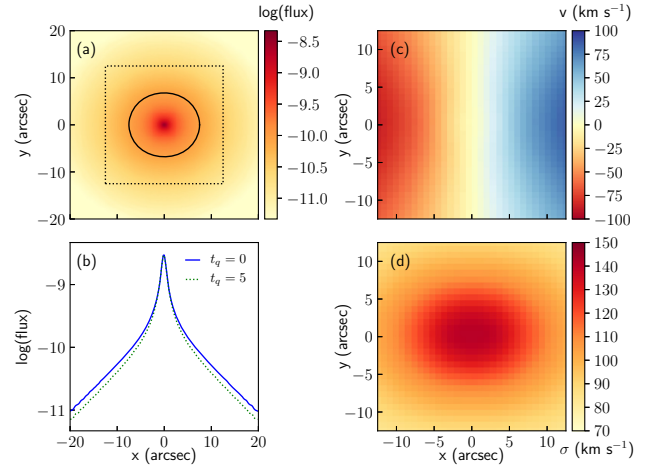

Figure 1. An example model with $B/T = 0.5$, inclination $= 30°$, and $t_q = 0$ Gyr. We show (panel a) the r-band flux image on a log-scale with a 1-R_e ellipse (solid line) and the region where the kinematics is simulated (dotted square); (panel b) the flux profile cut along the major axis (blue line solid; units are SDSS maggies), compared to the flux profile for the same model at $t_q = 5$ Gyr (green dotted line); (panel c) the stellar velocity map; and (panel d) the stellar velocity dispersion map.

(G79635) in Taranu et al. (2017) using images from the Kilo-Degree Survey (KiDS; Kuijken et al. 2019). While the differential between the g- and r-band FWHMs is larger than between the median values of 0.69 and 0.88 arcsec reported in KiDS DR4, it is not unusual for weak lensing-focused optical surveys to optimize r-band seeing over bluer bands.

An example of the simulated maps is shown in Fig. 1. In this case, we show the r-band image, velocity, and dispersion maps for a model galaxy with $B/T = 0.5$, inclination $= 30°$, and a quenching time of $t_q = 0$ Gyr. We also compare the flux profile to a model with $t_q = 5$ Gyr in Fig. 1(b).

2.3 Measuring effective radius, concentration, and λ_R

Our primary aim is to assess the impact of disc fading on the observed dynamical properties of galaxies. Given this, it is important that we apply the same measurement techniques to our models as is normally applied to real observations.

A robust and standard approach to measuring the effective radius, R_e, of a galaxy is via Multi-Gaussian Expansion (MGE; Emsellem, Monnet & Bacon 1994; Cappellari 2002). We apply this method to the synthetic r-band images, taking into account the applied seeing convolution to derive an MGE model of the unconvolved galaxy. Our models, that are projected to a range of inclinations, allow us to test which particular R_e estimates are most robust. Comparisons between different approaches are shown in Fig. 2. As pointed out by Cappellari et al. (2013), circularizing the MGE model and then correcting for the ellipticity to get a major axis R_e value leads to systematically lower R_e values at high inclination (red line in Fig. 2). Cappellari et al. (2013) provide a much better approach that uses the MGE model of each galaxy and identifies the isophote containing half of the model light. R_e is then defined as the maximum radius enclosed within that isophote, analogous to the major axis of an ellipse (blue line in Fig. 2). This maximum isophotal method shows much less variation with inclination, in agreement with Cappellari et al. (2013). However, at $I = 90°$, the maximum isophotal method shows a systematic offset to give larger
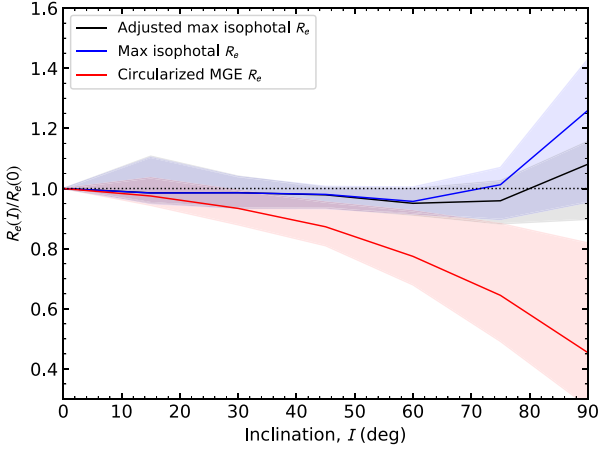
Figure 2. The variation of measured major axis R_e as a function of inclination, I. We show the ratio of R_e measured from a model at a given inclination to the value for $I = 0°$. The solid lines are the median over all models (full range of B/T and t_q) as a function of inclination while the shaded regions show the full range of R_e ratios. Three different R_e measurements are shown: a circularized MGE model (red), maximum isophotal radius (blue), and adjusted maximum isophotal radius (black).

R_e values. This offset is because in cases with a significant bulge and a thin edge-on disc the isophotes at $1R_e$ are far from elliptical. Much less deviation is found if we adjust the maximum isophotal R_e so that it is the major axis radius of an ellipse with the same area and ellipticity as the half-light isophote (black line in Fig. 2). Specifically, this adjusted maximum isophotal half-light radius, $R_{e, adj}$, is given by

$$R_{e,adj} = R_{e,iso}\sqrt{\frac{A_{iso}}{\pi R_{e,iso}^2(1 - \epsilon_{e,iso})}} = \sqrt{\frac{A_{iso}}{\pi(1 - \epsilon_{e,iso})}}, \quad (5)$$

where $R_{e, iso}$ is the maximum half-light isophotal radius, A_{iso} is the area within the half-light isophote, $\epsilon_{e, iso}$ is the ellipticity within the half-light isophote (based on a moments of inertia analysis), and $\pi R_{e,iso}^2(1 - \epsilon_{e,iso})$ is the area of an ellipse with semi-major axis of $R_{e, iso}$ and ellipticity $\epsilon_{e, iso}$. When the half-light isophotes are close to elliptical (which is true for almost all inclinations), then $R_{e, iso}$ and $R_{e, adj}$ are equivalent. Only near edge-on ($I = 90°$) do they diverge, with $R(I)_{e, iso}$ increasingly larger than the value at $I = 0°$. From here on, we use $R_{e, adj}$ for our half-light radius estimate for the simulations and will drop the adj subscript. We note that using $R_{e, iso}$ or $R_{e, adj}$ makes no significant difference to our conclusions in this paper.

Various authors have compared dynamical measurements (e.g. λ_R) to galaxy concentration (e.g. Fogarty et al. 2015; Querejeta et al. 2015). In these works the authors use the common SDSS definition of concentration, $C_p = r_{p, 90}/r_{p, 50}$, where $r_{p, 50}$ and $r_{p, 90}$ are the circular radii containing 50 and 90 per cent of the Petrosian flux, respectively (Strateva et al. 2001). To maintain consistency with these previous works, we also use this definition of concentration. A concentration of $C_p \gtrsim 2.5$ is typical of ellipticals and early-type galaxies, while $C_p \lesssim 2.5$ is typical for galaxies dominated by an exponential disc. In SDSS (and other surveys) the measurement of C_p is made on the seeing convolved images, so we do the same for our simulations. The one difference is that instead of using the Petrosian flux to derive the apertures we use the total MGE model flux, and so measure $C_m = r_{m, 90}/r_{m, 50}$ from the seeing convolved MGE model, where $r_{m, 50}$ and $r_{m, 90}$ are the circular radii containing 50 and 90 per cent of the total MGE model flux. The resulting distribution of C_m for

the model galaxies is consistent with the observed distribution of C_p from SDSS.

Finally, we measure λ_R from the seeing convolved model kinematic maps using

$$\lambda_R = \frac{\sum_{i=1}^{N} F_i R_i |V_i|}{\sum_{i=1}^{N} F_i R_i \sqrt{V_i^2 + \sigma_i^2}}, \quad (6)$$

where the summation is over all spaxels (1–N) that are contained within an elliptical aperture with semi-major axis and ellipticity of R_e and ϵ_e, respectively. F_i, V_i, and σ_i are the measured flux, velocity, and velocity dispersion in the ith spaxel. The radius to the ith spaxel, R_i, is defined to be the semi-major axis of the ellipse that the spaxel lies on (e.g. see Cortese et al. 2016; van de Sande et al. 2017b).

3 SIMULATION RESULTS

3.1 Simulated λ_R and concentration

The suite of models described above sample inclination ($i = 0°$, $15°$, $30°$, $45°$, $60°$, $75°$, $90°$), bulge-to-total mass ratio ($B/T = 0.0–1.0$ in steps of 0.1), and the time since quenching started ($t_q = 0, 1, 2, 3, 4$, and 5 Gyr). In Fig. 3 we display our models in the commonly used λ_R–ellipticity plane. For clarity we only include models with $B/T = 0.1, 0.3, 0.5, 0.7$, and 0.9. The models are compared to simple analytic descriptions of the expected tracks of oblate rotating galaxies in the λ_R–ellipticity plane that are described by Emsellem et al. (2011) and Cappellari et al. (2007), and which we will outline here for completeness. The relation between observed ellipticity, ϵ, and intrinsic ellipticity, ϵ_i, is given by

$$\epsilon_i = 1 - \sqrt{1 + \epsilon(\epsilon - 2)/\sin(I)^2}, \quad (7)$$

where I is the inclination. Cappellari et al. (2007) give the approximation that

$$V/\sigma = \sqrt{(0.09 + 0.1\epsilon_i)\epsilon_i/(1 - \epsilon_i)}. \quad (8)$$

This can then be converted into λ_R using the relation defined by Emsellem et al. (2007, see their appendix B) that incorporates a scaling factor κ,

$$\lambda_R = \frac{\kappa(V/\sigma)}{\sqrt{1.0 + [\kappa(V/\sigma)]^2}}. \quad (9)$$

van de Sande et al. (2017a) found that $\kappa = 0.97$ for SAMI galaxies, slightly different to the value of 1.1 found by Emsellem et al. (2011) from ATLAS3D. This difference is based on the use of elliptical radius for SAMI measurements of λ_{R_e}, while ATLAS3D uses circularized radius. The λ_R value at a given inclination is given by

$$\lambda_{R,inc} = \frac{C_i \lambda_R}{\sqrt{1 + (C_i^2 - 1)\lambda_R^2}}, \quad (10)$$

where C_i is defined by

$$C_i = \frac{\sin(I)}{\sqrt{1 - \beta_z \cos(I)^2}}. \quad (11)$$

We take the anisotropy parameter, $\beta_z = 0.7\epsilon_i$ (Cappellari et al. 2007; Cappellari 2016). Models tracks using the above formalism are shown in Fig. 3 by the magenta lines.

Our simulated galaxies with varying B/T and quenching time are shown by the coloured points in Fig. 3 (an example is also listed in Table 1). Different colours denote time since quenching, t_q, from 0 (magenta) to 5 Gyr (red). Simulated galaxies with only a small bulge
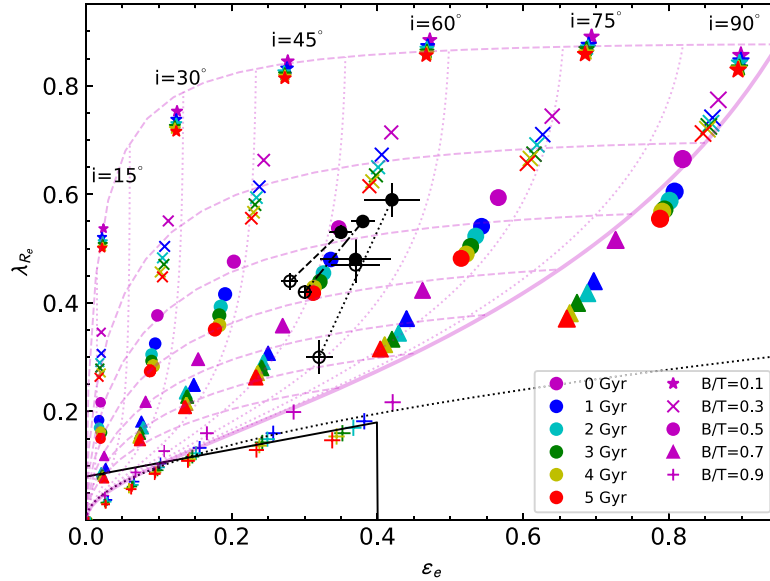
Figure 3. The distribution of our simulated galaxies in the λ_R–ellipticity plane. We show galaxy models with $B/T = 0.1$ (stars), 0.3 (crosses), 0.5 (circles), 0.7 (triangles), and 0.9 (pluses). The colours of symbols correspond to time since quenching of 0 (magenta), 1, (blue), 2 (cyan), 3 (green), 4 (yellow), and 5 (red) Gyr. The different sets of diagonal tracks correspond to different inclinations, $i = 15°$, $30°$, $45°$, $60°$, $75°$, and $90°$ (left to right), with point sizes becoming smaller for lower inclination. The black lines denote typical demarcations between fast and slow rotator of $\lambda_R = 0.31\sqrt{(\epsilon)}$ (dotted line; Emsellem et al. 2011) and $0.08 + 0.25\epsilon$ for $\epsilon < 0.4$ (solid line; Cappellari 2016). The magenta lines show the expected relations between λ_R and ellipticity for oblate rotators with anisotropy $\beta_z = 0.7\epsilon_i$. The solid magenta line is for edge-on galaxies with varying intrinsic ellipticity, ϵ_i; the magenta dotted lines are the same model, but with different inclinations (from $10°$ to $80°$); the magenta dashed lines show how galaxies with fixed intrinsic ellipticity (between 0.35 and 0.85) change with inclination. The black connected points show the mean values for early spiral, eSp, (filled circle) and S0 (empty circle) galaxies from SAMI after beam-smearing correction in the mass range $\log (M_*/M_\odot) = 9.5$–10.0 (solid line), 10.0–10.5 (dashed line), 10.5–11.0 (dot–dashed line), and 11.0–11.5 (dotted line).

contribution (e.g. $B/T = 0.1$, as indicated by a star symbol in Fig. 3) show little change in their location in the λ_R–ellipticity space as their disc fades. This is as expected given that the dominant component is always the disc. However, for galaxies with a significant bulge, we see substantial variations in both their λ_R and ellipticity as they age. For a galaxy with $B/T = 0.5$ (circles in Fig. 3) the change in λ_R is $\simeq$ 0.1 (with some dependency on inclination) across the 5 Gyr of disc fading that we model. There is also a small reduction in ellipticity as the spherical bulge component contributes a larger fraction of the light at late times. As we further increase B/T, the changes in λ_R decline again because these galaxies start with low λ_R and ellipticity, due to being dominated by their bulge, and so the influence of the fading disc is relatively small. The impact of disc fading is most strongly felt when the bulge and disc contribute similar amounts of light to the overall galaxy, as would be expected qualitatively.

The disc fading causes the galaxies to approximately follow the dotted magenta lines in Fig. 3. These trace lines of constant inclination for a varying intrinsic ellipticity. While these lines are derived for a single component oblate rotator, our bulge + disc models can be approximated by these lines with decreasing intrinsic ellipticity as the disc fades. Some models fall below the limiting case of an edge-on oblate rotator (solid magenta line), and these are the edge-on cases with large dispersion-dominated bulge components. In fact, for $B/T = 0.9$, our edge-on models fall into the slow rotator region, as defined by various different boundaries (Emsellem et al. 2011; Cappellari 2016). This is not surprising, given that our modelled bulge components are spherical and completely dispersion dominated, with no rotation. However, we note that the edge on $B/T = 0.9$ models can still have reasonably high ellipticity (up to $\epsilon_e = 0.4$). The reason for this high ellipticity is that the discs have a lower mass-to-light ratio than the bulge, and, when seen

edge-on, have higher surface brightness due to integrating through the disc.

Part of the change in measured spin in our models with time is due to a reduction in the measured R_e as the smaller bulge becomes more dominant as the disc fades. The fractional quantitative change in R_e is shown in Fig. 4, relative to the R_e of each model at $t_q = 0$ Gyr. The change in R_e is relatively modest, being $\simeq$ 10 per cent after 5 Gyr for a $B/T = 0.5$. For different B/T, the change in R_e is less than this. We will discuss the role of size evolution further below.

Placing our simulated galaxies in the λ_R–concentration plane (Fig. 5), we see that the change in λ_R is accompanied by a change in concentration. For a given inclination (signified by point size), the simulated galaxies lie along a diagonal track in this plane, with the gradient depending on inclination. Face on galaxies (small points) always have small λ_R, while edge-on galaxies show the largest change in λ_R. The position of a galaxy along a diagonal track (for a given inclination) is mostly defined by the light-weighted B/T in the SAMIgr band. This ratio is a combination of the mass-weighted B/T and the M/L of each component. As expected, given the above discussion, the largest change is for the edge-on case with a mass-weighted $B/T \simeq 0.5$. In this case, the change in λ_R is $\simeq$ 0.1, and the change in concentration is also $\simeq$ 0.1 for 5 Gyr of disc fading. As the galaxies become more face-on (smaller points at lower λ_R), the change in concentration becomes larger.

We can compare our models to results from simulations that contain dynamical interactions. Fogarty et al. (2015), using the simulations of BC11, find a change in λ_R from 0.77 to 0.47 and in concentration from 2.36 to 3.71, for an edge on model that starts with a B/T of 0.14 by mass. This model interacts with galaxies within a group for 5.6 Gyr. While the trends in our work and BC11 are qualitatively similar, BC11 shows larger changes in the observable

Table 1. Simulation results for the example of $B/T = 0.5$ and a range of inclinations (Inc) and quenching times (t_q).

B/T	Inc (°)	t_q (Gyr)	R_e (arcsec)	ϵ_e	λ_{R_e}	$(V/\sigma)_e$	R_{90}/R_{50}
0.5	0	0.0	7.71	0.00	0.00	0.00	2.40
0.5	0	1.0	7.42	0.00	0.00	0.00	2.46
0.5	0	2.0	7.26	0.00	0.00	0.00	2.49
0.5	0	3.0	7.15	0.00	0.00	0.00	2.51
0.5	0	4.0	7.07	0.00	0.00	0.00	2.53
0.5	0	5.0	7.00	0.00	0.00	0.00	2.55
0.5	15	0.0	7.93	0.02	0.22	0.19	2.40
0.5	15	1.0	7.64	0.02	0.18	0.16	2.47
0.5	15	2.0	7.50	0.02	0.17	0.15	2.50
0.5	15	3.0	7.41	0.02	0.16	0.14	2.52
0.5	15	4.0	7.83	0.02	0.16	0.14	2.54
0.5	15	5.0	7.24	0.02	0.15	0.13	2.55
0.5	30	0.0	7.83	0.10	0.38	0.37	2.43
0.5	30	1.0	7.56	0.10	0.33	0.31	2.49
0.5	30	2.0	7.47	0.09	0.30	0.29	2.52
0.5	30	3.0	7.41	0.09	0.29	0.28	2.54
0.5	30	4.0	7.36	0.09	0.28	0.27	2.56
0.5	30	5.0	7.28	0.09	0.27	0.26	2.57
0.5	45	0.0	7.58	0.20	0.48	0.51	2.47
0.5	45	1.0	7.24	0.19	0.42	0.43	2.53
0.5	45	2.0	7.10	0.18	0.39	0.40	2.55
0.5	45	3.0	7.01	0.18	0.38	0.38	2.57
0.5	45	4.0	6.94	0.18	0.36	0.36	2.59
0.5	45	5.0	6.86	0.18	0.35	0.35	2.60
0.5	60	0.0	7.33	0.35	0.54	0.64	2.54
0.5	60	1.0	7.09	0.34	0.48	0.55	2.60
0.5	60	2.0	6.95	0.33	0.46	0.51	2.62
0.5	60	3.0	6.86	0.32	0.44	0.49	2.64
0.5	60	4.0	6.76	0.31	0.43	0.47	2.66
0.5	60	5.0	6.78	0.31	0.42	0.46	2.67
0.5	75	0.0	7.48	0.57	0.59	0.79	2.75
0.5	75	1.0	7.17	0.54	0.54	0.68	2.79
0.5	75	2.0	7.12	0.54	0.52	0.65	2.81
0.5	75	3.0	7.03	0.53	0.50	0.62	2.82
0.5	75	4.0	6.95	0.52	0.49	0.59	2.83
0.5	75	5.0	6.89	0.52	0.48	0.58	2.84
0.5	90	0.0	8.32	0.82	0.67	0.95	2.97
0.5	90	1.0	8.12	0.81	0.60	0.84	3.01
0.5	90	2.0	8.05	0.80	0.59	0.80	3.03
0.5	90	3.0	7.92	0.79	0.57	0.77	3.05
0.5	90	4.0	8.03	0.79	0.57	0.76	3.06
0.5	90	5.0	7.96	0.79	0.56	0.74	3.07

Note. Other B/T ratios are available in the electronic version of this paper.

parameters, particularly in concentration. Given that the bulge mass is a small fraction of the total in the BC11 simulations, any contribution to their results from disc fading should be small. For example, we would expect the impact to be less than the change seen in the crosses in Fig. 5, which has a B/T of 0.3 by mass.

3.2 Testing possible systematic effects

The above suite of simulations provides a set of galaxies that broadly matches the observed properties of the galaxy population. However, a number of observational and physical effects can potentially modify the measured quantities. Here we will discuss these in turn. Below we will generally make comparisons to our fiducial model set (described above) for a galaxy with $B/T = 0.5$ and inclination of $45°$.

The first potential systematic we consider is the impact of atmospheric seeing. The simulated λ_{R_e} values are measured from
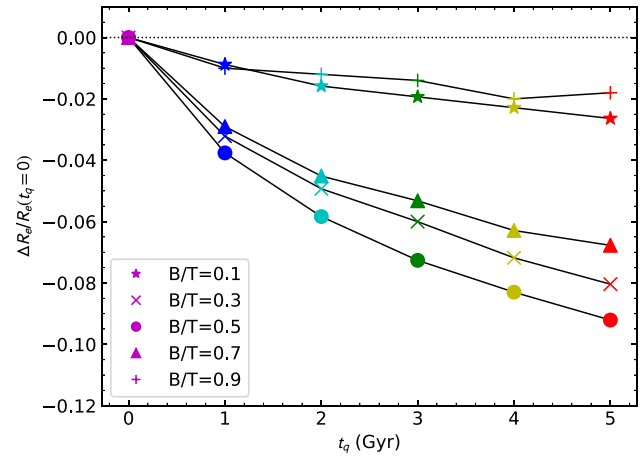

Figure 4. The fractional change in R_e as a function of quenching time in our models for different B/T ratios. The change in R_e is shown as $\Delta R_e = R_e(t_q) - R_e(t_q = 0)$, normalized by $R_e(t_q = 0)$. Each point is the median over all inclinations that have been modelled. Symbol types and colours are the same as in Fig. 3. Objects with $B/T = 0.5$ show the greatest change in size.

models that have not been convolved with the seeing (as we correct our SAMI galaxy measurements for beam-smearing). In contrast, we measure concentration after convolution with the seeing, as this matches the measurements made on the data. To quantify the impact of these choices, we compare our simulation results with and without seeing convolution. When we do this, we find that λ_{R_e} changes from 0.41 (for SAMI-like seeing) to 0.48 (native simulation resolution) for our fiducial model of $B/T = 0.5$ and inclination of $45°$ at $t_q = 0$ Gyr. This difference is typical of the impact of seeing on λ_{R_e} measurements (Graham et al. 2018; Harborne et al. 2019, 2020a) for galaxies at this spatial resolution (the ratio of seeing σ to R_e is approximately 0.2). While there is an overall decrease in λ_{R_e} in the presence of seeing, the relative evolution of λ_{R_e} due to disc fading is hardly changed. In our no seeing case, 5 Gyr of disc fading gives $\Delta\lambda_{R_e} = \lambda_{R_e}(t_q = 5\text{Gyr}) - \lambda_{R_e}(t_q = 0) = -0.116$, while for SAMI-like seeing, this is $\Delta\lambda_{R_e} = -0.118$. Concentration is less affected by seeing and we find that our fiducial model with $t_q = 0$ Gyr has concentration $C = 2.477$ for no seeing and $C = 2.471$ for SAMI-like seeing. The change in concentration with disc fading is also unaffected with $\Delta C = C(t_q = 5\text{Gyr}) - C(t_q = 0) = 0.135$ (for no seeing) and $\Delta C = 0.134$ (for SAMI-like seeing).

The second observational effect is the signal-to-noise ratio (S/N) of the measurement. We have assumed perfect data in constructing our models, but changes in S/N could impact the measured parameters. To examine this, we generate one set of galaxies (with $B/T = 0.5$ and inclination of $45°$) with S/N typical of KIDS imaging and SAMI spectroscopic observations. We then measure λ_{R_e} and concentration for these simulations with added noise. The difference caused by adding noise to the simulations is found to be at most $\simeq 1.3$ per cent in λ_{R_e} and concentration. We also test how the S/N influences our measurement of $\Delta\lambda_{R_e}$ and ΔC. These are similarly small, with the difference in $\Delta\lambda_{R_e}$ being 0.9 per cent and the difference in ΔC being 1.6 per cent. These changes are much smaller than the trends we find due to disc fading and as a result we do not consider the effect of S/N for the remainder of this paper.

Another alternative is that the disc scale-height could vary with disc size. We introduce a varying disc scale-height that is one-eighth of the disc scale-length, varying from the fiducial value ($z_d = 0.75$ kpc) for the most massive discs to about half of this value for
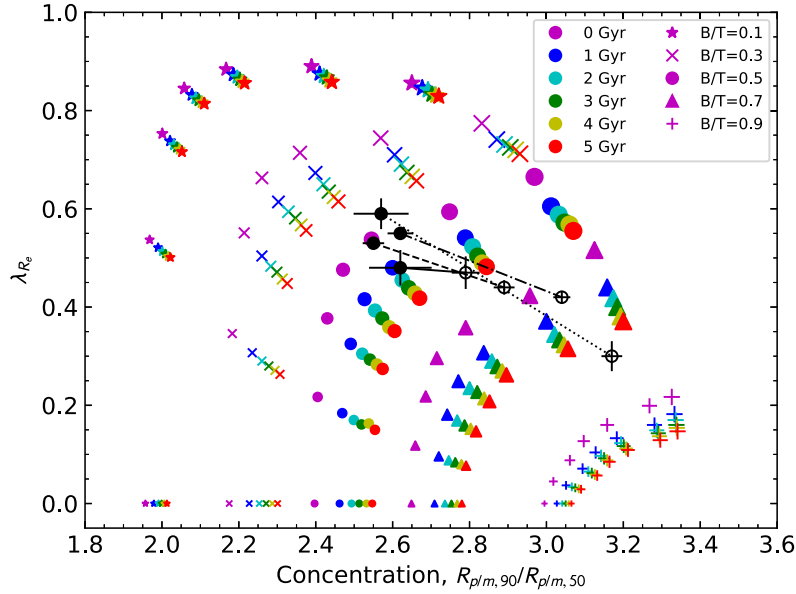
Figure 5. The distribution of our model galaxies in the λ_{R_e}–concentration plane. The colours, sizes and shapes of the points are identical to Fig. 3. In this figure, we also include galaxies at inclination $i = 0°$, which all lie at $\lambda_{R_e} = 0$. As the inclination increases, the model tracks become steeper and have higher λ_{R_e} and higher concentration.

the least massive. The result is only a minimal change in our results, with average changes between the fiducial model and the varying scale height model being 0.022 in λ_{R_e}, 0.008 in $\Delta\lambda_{R_e}$, -0.045 in concentration, and -0.011 in ΔC.

Variations in dust content between early- and late-type galaxies could influence our measurements. The amount of extinction due to dust is found to be dependent on stellar population age (e.g. Cortese et al. 2008). Disc scale-lengths have been shown to be colour dependent (e.g. Peletier et al. 1994; de Grijs 1998), and this has been explained by the distribution of dust in discs. However, more recent measurements of disc scale-lengths as a function of wavelength in large samples spanning a range of inclinations and other galaxy properties show weaker evidence for wavelength dependence (Fathi et al. 2010). Early-type galaxies can contain significant amounts of dust, but this is typically much less than late-type galaxies (e.g. Smith et al. 2012; Beeston et al. 2018). Simulations including the impact of dust (e.g. Gadotti, Baes & Falony 2010; Pastrav et al. 2013) on observed properties find that dust tends to lower the B/T, and make discs appear larger, with the degree of change depending on the assumed optical depth and dust geometry. If the star-forming spirals contain significantly more dust than S0s, this would increase the observed difference in λ_{R_e} and concentration. However, given the difficulty of quantifying the differential impact of dust between spirals and S0s, we choose not to implement a dust correction in our models.

4 SAMI GALAXIES IN THE λ_{R_e}–CONCENTRATION PLANE

4.1 SAMI galaxy measurements

The SAMI instrument (Croom et al. 2012) uses 13 deployable imaging fibre bundles (hexabundles; Bland-Hawthorn et al. 2011; Bryant et al. 2014) across a $1°$ diameter field of view at the prime focus of the 3.9-m Anglo-Australian Telescope. The hexabundles each contains 61 fibres, and each fibre is 1.6 arcsec in diameter. Each

hexabundle therefore covers a circular 15 arcsec diameter region on the sky, with a filling factor of 75 per cent. The SAMI fibres are fed to the dual-beam AAOmega spectrograph (Sharp et al. 2006).

The SAMI Galaxy Survey (Croom et al. 2012; Bryant et al. 2015) targeted over 3000 galaxies from 2013 to 2018 and covers a broad range in stellar mass ($\log(M_*/M_\odot) = 10^8$–10^{12}) in the redshift range $0.004 < z < 0.095$. Targets were selected based on SDSS photometry and spectroscopy from the Galaxy And Mass Assembly survey (GAMA; Driver et al. 2011). A further eight high-density cluster regions were also targeted to capture the richest environments (Owers et al. 2017). In the current analysis we include the SAMI cluster fields, but only those that have SDSS imaging (Abell clusters 168, 2399, 119, and 85), to maintain a consistent of photometric measurements, particularly concentrations.

The spectroscopic observations from the SAMI Galaxy Survey cover the wavelength ranges 3750–5750 and 6300–7400 Å, at a resolution of $R = 1808$ and 4304 at the spectral wavelengths of 4800 and 6850 Å, respectively (van de Sande et al. 2017b; Scott et al. 2018).

The data is reduced using a combination of the 2dFdr fibre reduction code (AAO software team 2015) and a purpose built pipeline (Allen et al. 2014). A detailed description is given by Sharp et al. (2015) and Allen et al. (2015). The resulting data products are wavelength-calibrated, sky-subtracted, and flux-calibrated spectral cubes. The cubes are generated separately for the red and blue spectrograph arms.

The simulations do not include any AGN contribution, but bright nuclear continuum from an AGN could alter the observed concentration measurements. We visually check the nuclear spectra (3-arcsec diameter aperture) of all SAMI galaxies. Only 11 objects from the entire sample show evidence of broad emission lines that would suggest the nucleus is not obscured. Of these, only two objects (SAMI catalogue IDs 376679 and 718921) have a significant non-stellar continuum and we exclude these from our analysis below.

To compare our disc fading models to data, we use stellar kinematics from the SAMI Galaxy Survey, and specifically internal

Data Release 0.12 that contains 3071 unique galaxies from the completed survey. These data products are identical to those released in SAMI Data Release 3 (Croom et al. 2021). Only using cluster galaxies that have SDSS imaging discounts 321 galaxies in fields with only VST-ATLAS Survey imaging (Shanks et al. 2015). As a result 597 cluster galaxies with SDSS imaging are potential objects to still include in our analysis.

Stellar kinematics are measured using the penalized pixel fitting routine, PPXF (Cappellari & Emsellem 2004), following the method discussed in detail by van de Sande et al. (2017b). We will only highlight key points of the fitting here, and refer the reader to van de Sande et al. (2017b) for further details. The red arm data are convolved to match the blue in terms of spectral resolution and then the two arms are fitted simultaneously, assuming a Gaussian line-of-sight velocity distribution. Optimal templates are derived by fitting annularly binned spectra using the MILES stellar library (Sánchez-Blázquez et al. 2006). PPXF is then run on individual spaxels in three passes, first to measure the noise from residuals, then to clip outlying pixels and emission lines, and finally to derive the kinematic parameters. On the third pass, PPXF uses a linear combination of the optimal template in the relevant annulus and those in the adjacent annuli. Uncertainties for each spectral measurement are estimated from fits to 150 simulated spectra, where noise is added that is consistent with the observations.

Based on the above fitting, we then apply the quality cuts suggested by van de Sande et al. (2017b), namely S/N > 3 Å^{-1}; σ_{obs} > FWHM$_{instr}$/2 $\simeq$ 35 km s^{-1}; V_{error} < 30 km s^{-1}; and σ_{error} < σ_{obs}*0.1 + 25 km s^{-1}. The R_e, PA, and ellipticity of each SAMI galaxy is measured in the same way as the models described in Section 2.3, using MGE (Emsellem et al. 1994; Cappellari 2002; Scott et al. 2009). Detailed application of this to the SAMI data is described by D'Eugenio et al. (2021). Similarly, λ_{R_e} is also measured following the procedure in Section 2.3. We include galaxies where the λ_{R_e} measurement is aperture corrected to 1R_e (van de Sande et al. 2017a), in cases where the SAMI data do not extend to 1R_e.

For data taken at the spatial resolution of SAMI, seeing can impact the kinematic measurements. This 'beam-smearing' tends to convert velocity into dispersion and hence lower λ_{R_e}. Various authors have developed beam-smearing corrections for λ_{R_e} (e.g. Graham et al. 2018). We use the newly derived corrections by Harborne et al. (2020a). These corrections are derived by applying observational features to an array of simulated galaxies using the SIMSPIN software (Harborne, Power & Robotham 2020b). The corrections are a function of σ_{PSF}/R_e, ellipticity, and Sérsic index where σ_{PSF} describes the width of the observational point spread function. We only use galaxies where σ_{PSF}/R_e < 0.5, to minimize any residual impact of beam smearing. After correction, Harborne et al. (2020a) find that the dispersion in λ_{R_e} between the true and beam-smearing corrected simulations is only 0.026 dex and the mean is only different by 0.001 dex. Beam-smearing corrections are particularly important in this work because they are dependent on galaxy size. Early-type galaxies are, on average, smaller than late-type galaxies, so beam-smearing could cause systematic differences. Applying all the kinematic quality cuts results in a sample of 1595 galaxies.

Optical morphological classification of SAMI galaxies is described in detail by Cortese et al. (2016). The classification uses SDSS DR9 (Ahn et al. 2012) colour images inspected by at least eight independent members of the team. First the galaxies were subdivided into early or late type, based on the presence of spiral arms and/or indications of star formation. The galaxies were then further subclassified and given an index that we call mtype, from 0 to 3. Early-type galaxies were further categorized as elliptical (E,

mtype = 0) or lenticular (S0, mtype = 1) based on the presence of a disc. Late-type galaxies were subdivided into those with a bulge (early spiral eSp, mtype = 2) or without a bulge (late sprial, lSp, mtype = 3). At least 66 per cent agreement was required for these classifications. If this was not met, then adjacent votes were combined into intermediate classes with mtype = 0.5, 1.5, or 2.5. If there is still no agreement reached, the galaxy is unclassified. Removing galaxies that are morphologically unclassified from our kinematic sample, we then have 1566 galaxies.

Optical concentrations are taken from SDSS DR7 (Abazajian et al. 2009), and are based on the standard definition of $C_p = r_{p, 90}/r_{p, 50}$, where $r_{p, 50}$ and $r_{p, 90}$ are the circular radii containing 50 and 90 per cent of the Petrosian flux, respectively (Strateva et al. 2001). We find one galaxy that does not have a valid concentration (i.e. bad values or photometric flags from SDSS), resulting in a final sample of 1565 galaxies.

4.2 Trends in λ_{R_e} and concentration with morphology and mass for SAMI galaxies

The distribution of SAMI galaxies in the λ_{R_e}–concentration plane is shown in Fig. 6. To distinguish mass trends from other effects, we separate the galaxies into bins of 0.5 dex in log($M_*/M_\odot$). At masses below log($M_*/M_\odot$) = 10, there are a smaller number of galaxies and the range of morphologies is more limited. One aspect of this is the purely physical effect that most low-mass galaxies are late-type spirals or irregulars. However, another factor is that the lower surface brightness for these galaxies means that the measured stellar kinematics is less complete at low masses. In Fig. 7, we show the stellar kinematic completeness as a function of mass and below log($M_*/M_\odot$) = 9.5 this drops quickly. However, above log($M_*/M_\odot$) = 10.0, our stellar kinematic measurements are relatively complete, and we also have a broad range of morphology. The above points highlight the need to make consistent comparisons at the same stellar mass when investigating morphology trends.

When we subdivide our sample by morphology (mtype) at log($M_*/M_\odot$) > 9.5 (colour-coded in Fig. 6 from purple to red for late to early type), we see the expected trends that earlier galaxy types (lower mtype value) have higher concentration and lower λ_{R_e}. While there is significant scatter (in part caused by inclination), the mean trends (large points) are clear. The mean values are also given in Table 2 (note that we only give mean values when we have at least five galaxies in a mass–morphology bin).

Our main aim in this paper is to test whether the changes seen when spirals transition to S0 galaxies could be consistent with disc fading. For this, it is best to define samples that are minimally contaminated with other morphologies, that could bias our measurements. We therefore now consider only those objects for which the morphology is classified as S0 with mtype = 1 (yellow points in Fig. 6). We do not include objects with morphological classifications of mtype = 0.5 or 1.5, as these intermediate classes were only assigned when agreement could not be reached in our classification. Therefore, they likely contain contamination from adjacent morphological classes.

As the comparison to our S0s we take the SAMI objects classified as pure early-type spiral galaxies, mtype = 2 (light blue points in Fig. 6). We make this choice because this class should be minimally contaminated by S0s, have significant numbers across each of the mass intervals above log($M_*/M_\odot$) = 10.0, and, based on their classification, should show evidence for a bulge. That said, we note that the mtype = 2.5 or 3.0 classes are generally close to the mtype = 2.0 galaxies in the λ_{R_e}–concentration plane. If anything,
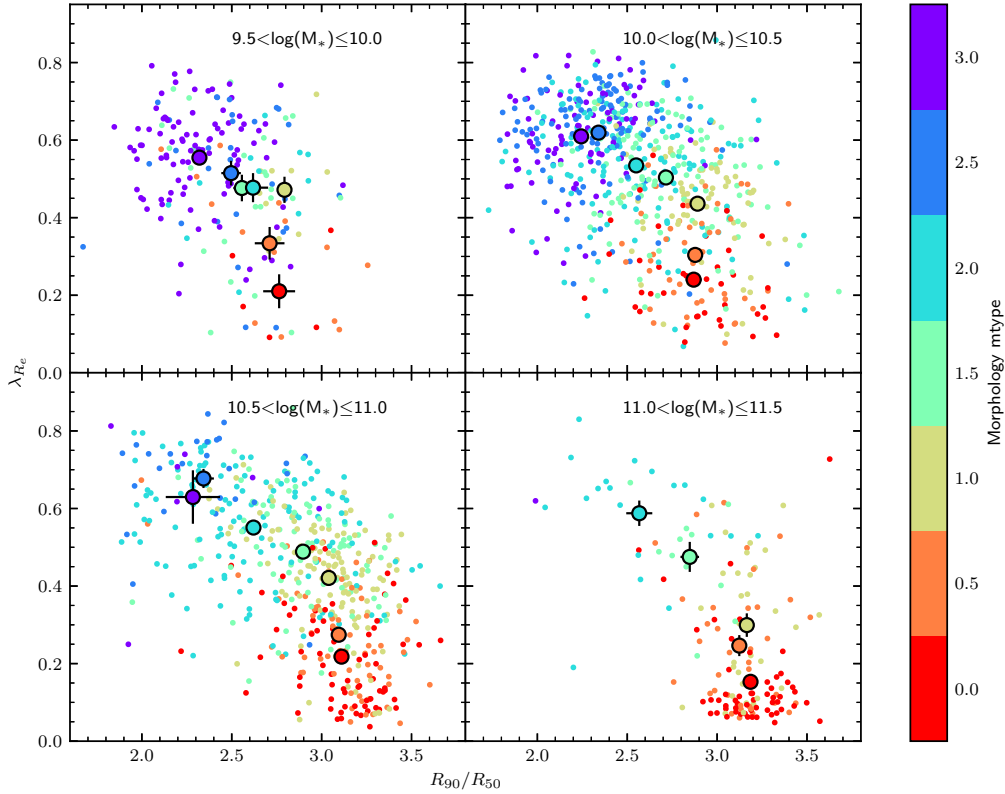
Figure 6. The distribution of our SAMI galaxies in the λ_R–concentration plane (corrected for seeing effects). Galaxies are separated into 0.5-dex intervals of stellar mass and then colour-coded by morphology (small points) from mtype = 0 (ellipticals, red points) to 3 (late spirals, purple points). The large points show the mean λ_R and concentration values for each morphology, and are only plotted when there are at least five galaxies to average. The error bars on the large points show the error on the mean and are often smaller than the points.
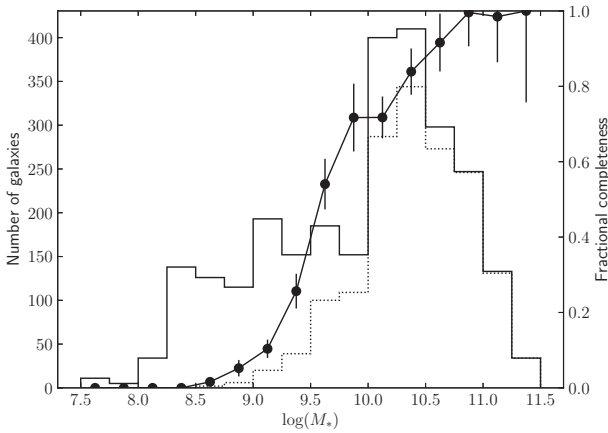

Figure 7. The stellar mass distribution of our SAMI galaxies for all objects (solid histogram) and objects for which we have robust stellar kinematics (dotted histogram). Also shown (circles with error bars; right axis) is the fractional completeness of the stellar kinematic sample as a function of mass.

the later mtypes have slightly higher λ_{R_e} and lower concentration, so looking at the difference between mtype = 2.0 (early spiral, eSp) and 1.0 (S0) provides a lower limit on the global difference between spirals and S0s.

The values of $\Delta\lambda_{R_e} = \lambda_{R_e}(eSp) - \lambda_{R_e}(S0)$ and $\Delta C = C(eSp) - C(S0)$ are listed in Table 3. In all three mass intervals above $\log(M_*/M_\odot) = 10.0$, the difference in concentration and λ_{R_e} between

Table 2. The mean λ_R, concentration (R_{90}/R_{50}), and ellipticity (e) for SAMI galaxies separated by mass [in 0.5 bins of $\log(M_*/M_\odot)$] and morphological mtype.

$\log(M_*)$	mtype	N_g	$\overline{\lambda_R}$	$\overline{R_{90}/R_{50}}$	$\overline{e}$
9.5–10.0	0.0	6	0.210 ± 0.044	2.764 ± 0.089	0.100 ± 0.026
9.5–10.0	0.5	15	0.334 ± 0.042	2.711 ± 0.083	0.127 ± 0.023
9.5–10.0	1.0	11	0.472 ± 0.034	2.793 ± 0.038	0.369 ± 0.035
9.5–10.0	1.5	27	0.476 ± 0.034	2.556 ± 0.047	0.298 ± 0.032
9.5–10.0	2.0	11	0.477 ± 0.037	2.618 ± 0.084	0.366 ± 0.051
9.5–10.0	2.5	29	0.515 ± 0.032	2.496 ± 0.054	0.393 ± 0.037
9.5–10.0	3.0	96	0.555 ± 0.013	2.320 ± 0.025	0.417 ± 0.020
10.0–10.5	0.0	38	0.240 ± 0.019	2.870 ± 0.045	0.074 ± 0.010
10.0–10.5	0.5	48	0.304 ± 0.018	2.878 ± 0.030	0.131 ± 0.012
10.0–10.5	1.0	66	0.436 ± 0.015	2.891 ± 0.028	0.283 ± 0.011
10.0–10.5	1.5	112	0.504 ± 0.015	2.715 ± 0.029	0.345 ± 0.014
10.0–10.5	2.0	148	0.535 ± 0.012	2.550 ± 0.028	0.351 ± 0.016
10.0–10.5	2.5	126	0.619 ± 0.011	2.340 ± 0.024	0.436 ± 0.021
10.0–10.5	3.0	85	0.610 ± 0.013	2.244 ± 0.029	0.417 ± 0.025
10.5–11.0	0.0	74	0.218 ± 0.014	3.111 ± 0.029	0.103 ± 0.008
10.5–11.0	0.5	64	0.274 ± 0.017	3.095 ± 0.035	0.144 ± 0.009
10.5–11.0	1.0	118	0.421 ± 0.013	3.040 ± 0.022	0.299 ± 0.009
10.5–11.0	1.5	90	0.489 ± 0.014	2.896 ± 0.029	0.380 ± 0.016
10.5–11.0	2.0	138	0.551 ± 0.012	2.621 ± 0.033	0.379 ± 0.016
10.5–11.0	2.5	27	0.677 ± 0.025	2.343 ± 0.058	0.478 ± 0.040
10.5–11.0	3.0	7	0.630 ± 0.069	2.284 ± 0.151	0.291 ± 0.095
11.0–11.5	0.0	59	0.153 ± 0.016	3.186 ± 0.025	0.112 ± 0.009
11.0–11.5	0.5	36	0.246 ± 0.027	3.123 ± 0.032	0.224 ± 0.017
11.0–11.5	1.0	31	0.299 ± 0.030	3.165 ± 0.027	0.319 ± 0.018
11.0–11.5	1.5	11	0.475 ± 0.039	2.848 ± 0.052	0.323 ± 0.043
11.0–11.5	2.0	20	0.588 ± 0.033	2.567 ± 0.072	0.416 ± 0.038

Note. Only bins where the number of galaxies (N_g) is 5 or greater are listed.

Table 3. The difference between mean λ_{R_e} and concentration (C) for different morphological or SFR-defined classes.

log (M_*)	$\Delta\lambda_{R_e}$ (S0-eSp)	ΔC (S0-eSp)	Significance $\Delta\lambda_{R_e}$	ΔC	Frac. DF $\Delta\lambda_{R_e}$	ΔC
		All Morph (S0-eSp)				
9.5–10.0	-0.006 ± 0.048	0.175 ± 0.088	-0.1	2.0	9.93	0.47
10.0–10.5	-0.099 ± 0.020	0.341 ± 0.039	-5.0	8.7	0.56	0.24
10.5–11.0	-0.130 ± 0.018	0.419 ± 0.040	-7.3	10.5	0.42	0.20
11.0–11.5	-0.288 ± 0.044	0.598 ± 0.075	-6.6	7.9	0.19	0.14
All	-0.132 ± 0.013	0.417 ± 0.026	-10.4	16.1	0.42	0.20
		No-SR Morph (S0-eSp)				
9.5–10.0	-0.006 ± 0.048	0.175 ± 0.088	-0.1	2.0	9.93	0.47
10.0–10.5	-0.097 ± 0.017	0.352 ± 0.039	-5.7	9.0	0.56	0.23
10.5–11.0	-0.098 ± 0.016	0.409 ± 0.040	-6.2	10.1	0.56	0.20
11.0–11.5	-0.220 ± 0.037	0.596 ± 0.079	-5.9	7.6	0.25	0.14
All	-0.104 ± 0.011	0.409 ± 0.026	-9.6	15.5	0.53	0.20
		No-SR SFR (INT-SF)				
9.5–10.0	-0.026 ± 0.033	0.100 ± 0.054	-0.8	1.8	2.14	0.91
10.0–10.5	-0.066 ± 0.018	0.194 ± 0.036	-3.6	5.4	0.85	0.47
10.5–11.0	-0.084 ± 0.019	0.301 ± 0.045	-4.3	6.6	0.67	0.30
11.0–11.5	-0.210 ± 0.038	0.403 ± 0.104	-5.5	3.9	0.27	0.23
All	-0.081 ± 0.011	0.309 ± 0.026	-7.3	12.1	0.69	0.29
		No-SR SFR (PAS-SF)				
9.5–10.0	-0.105 ± 0.022	0.272 ± 0.042	-4.7	6.4	0.53	0.34
10.0–10.5	-0.194 ± 0.012	0.445 ± 0.026	-15.9	16.8	0.29	0.20
10.5–11.0	-0.191 ± 0.016	0.517 ± 0.035	-12.3	14.8	0.29	0.18
11.0–11.5	-0.307 ± 0.037	0.603 ± 0.098	-8.3	6.1	0.18	0.15
All	-0.187 ± 0.008	0.506 ± 0.019	-22.6	26.8	0.30	0.18

Notes. This is shown in mass intervals for the difference between S0 (mtype = 1) and eSp (mtype = 2) galaxies, the different between INT and SF galaxies, and the difference between PAS and SF galaxies. Samples listed as 'No-SR' do not include slow rotators (which lie within the region defined by Cappellari 2016). We also list the significance of the difference and the fractional difference that can be contributed by disc fading. For the disc fading contribution, we compare to the model results averaged over all B/T and inclination values, of $\Delta\lambda_{R_e} = -0.056$ and $\Delta C = 0.091$. The last row for each sample contains the results for the full mass range between $\log(M_*/M_\odot) = 9.5$ and 11.5, based on an inverse variance weighted average of the individual mass bins.

eSp (mtype = 2) and S0 (mtype = 1) galaxies is highly significant. Taking the average across the full mass range ($\log(M_*) = 9.5$–11.5, although limiting to greater than 10.0 make no difference to the results), gives a mean $\Delta\lambda_{R_e} = -0.132 \pm 0.013$ and mean $\Delta C = 0.417 \pm 0.026$. In calculating the average across all masses, we take an inverse variance weighted average of the differences in each of the four separate mass intervals. This approach is more reliable than calculating the mean λ_{R_e} and concentration using a single large mass bin, as the changing morphological mix as a function of mass can bias the difference in this case.

There is a trend of increasing difference between eSp and S0 galaxies as mass increases for both λ_{R_e} and concentration. In λ_{R_e}, the trend with mass is largely driven by decreasing spin for S0 galaxies as mass increases. However, the main trend in concentration is increasing concentration as mass increases for S0 galaxies (Table 3). A natural interpretation of increasing concentration with mass is that higher mass S0s have a larger B/T. We do indeed see this trend in bulge-disc decomposition of GAMA galaxies (Casura et al. in preparation). However, the fact that we do not see equivalent changes in λ_{R_e} suggests that the bulges (or at least more concentrated components) still have substantial dynamical support from rotation. Future work will focus on explicit kinematic bulge-disc decomposition to explore this issue further.

Another possible contribution to the mass trends seen is the increased fraction of slow rotators above $\log(M_*/M_\odot) = 11.0$ (e.g. Brough et al. 2017; van de Sande et al. 2017a). The S0 sample could be contaminated by slow rotators at high mass, leading to lower spin measurement. At lower masses this contamination is unlikely

to be causing any offsets, given that the fraction of slow rotators is small. To directly test this, we recalculate our SAMI results but removing any galaxy that is within the slow rotator region defined by $\lambda_{R_e} < 0.08 + \epsilon/4$ and $\epsilon < 0.4$ (Cappellari 2016). The results of removing the slow rotators are shown in Table 3. Unsurprisingly, the eSp galaxies are unaffected by the slow rotator cut, as only 3 out of 317 eSp galaxies lie in the slow rotator region of the λ_{R_e}–ellipticity plane (face-on discs). The S0 galaxies are somewhat more impacted by removing slow rotators, particularly at high mass. This is either due to true S0s with lower average λ_{R_e} scattering into the slow rotator region, or intrinsically slow-rotating galaxies being misclassified as S0s as part of our morphological classification. Removing the slow rotators leads to a smaller overall change in λ_{R_e} with $\Delta\lambda_{R_e} = -0.104 \pm 0.011$ (slow rotators removed) compared to -0.129 ± 0.013 (retaining slow rotators) when averaged over all masses. In contrast, the concentrations are hardly affected with $\Delta C = 0.409 \pm 0.026$ (slow rotators removed) compared to 0.417 ± 0.026 (retaining slow rotators). For both λ_{R_e} and concentration, the difference between eSp and S0 galaxies is still highly significant, even when removing slow rotators.

4.3 Trends in λ_{R_e} and concentration for star-forming and passive fast rotators

Another consideration when looking at our comparison between eSp and S0 galaxies is whether optical morphology is the appropriate way to categorize such galaxies. There are clearly significant structural

and kinematic differences between eSp galaxies and S0 galaxies. However, classifying these galaxies based on the presence of spiral arms or a bulge may only be an indirect approach to identifying the primary physical differences between these populations. In almost all cases spiral arms will also signify star formation, as the enhanced star formation in the spiral arms leads to easier identification. The connection between morphology and star formation is well known (e.g. Davies et al. 2019). However, there are cases of redder spirals that have weak or undetected star formation (e.g. Pak et al. 2019). A more direct approach might be to simply compare star-forming and passive fast-rotating galaxies to assess the degree of dynamical evolution as the star formation is quenched.

To estimate current star formation in our SAMI galaxies we use the Hα emission-line maps. We remove regions that have non-star-forming line ratios in the [O III]/Hβ versus [N II]/Hα ionization diagnostic diagram (Baldwin, Phillips & Terlevich 1981), i.e. those spaxels that are significantly ($>1\sigma$) above the line defined by Kauffmann et al. (2003). We then sum the star-forming Hα flux and convert to SFR following a prescription similar to Medling et al. (2018). The Hα flux is corrected for internal extinction using a Balmer decrement averaged across the galaxy and then converted to an SFR using the conversion of Kennicutt, Tamblyn & Congdon (1994), but corrected to assume a Chabrier (2003) initial mass function. This estimate of star formation may underestimate the total SFR in some cases, such as when the star-forming disc extends beyond the SAMI field of view, or when non-star-forming spaxels rejected by ionization diagnostics still contain some star formation. However, our goal here is to broadly classify galaxies as star-forming or passive, and we find that our results are not sensitive to the details of the star formation estimate.

To classify our sample, we use a galaxy's location with respect to the star-forming main sequence. We use the local relation defined by Renzini & Peng (2015) such that $\log[SFR_{MS}/(M_* \, yr^{-1})] = (0.76 \pm 0.01)\log(M_*/M_\odot) - (7.64 \pm 0.02)$ with a scatter of 0.3 dex. We then define $\Delta(SFR) = \log(SFR_{MS}) - \log(SFR)$. Our star-forming population (labelled SF) is defined as galaxies that have $\Delta(SFR) > -0.6$ (twice the measured scatter). We define an intermediate population (labelled 'INT') with $-1.6 < \Delta(SFR) < -0.6$, and a passive population (labelled 'PAS') with $\Delta(SFR) < -1.6$. Our conclusions are not sensitive to the specific thresholds that we set for these categories.

The distribution of galaxies with λ_{R_e} measurements in the specific star formation rate (sSFR) versus mass plane can be seen in Fig. 8. With the points in Fig. 8 colour-coded by λ_{R_e}, a strong trend is visible, with galaxies at low sSFR typically having much lower λ_{R_e}. We classify galaxies as slow rotators based on the boundary defined by Cappellari (2016). These slow rotators are shown with black edges in Fig. 8 and are predominantly passive, although we note a small number of slow rotators that sit on the SFR main sequence.

The λ_{R_e}, concentration, and ellipticity values for the SAMI sample divided by SFR are listed in Table 4 and displayed in Fig. 9. Here we do not include objects classified as slow rotators, under the assumption that they follow a different formation pathway. The points in Fig. 9 are colour-coded by sSFR. At stellar masses above $\log(M_*/M_\odot) = 9.5$, there is a clear trend for galaxies with decreasing sSFR to have lower λ_{R_e} and higher concentration. This trend is as expected, given the trends we also see based on visual morphology.

Fig. 9 shows that the mean λ_{R_e} and concentration for galaxies classed as INT (large green points, with some residual star formation, but below the main sequence) are found between the SF galaxies (large blue points) and the PAS galaxies (large red points). The differences are quantified in the lower two sections of Table 3.
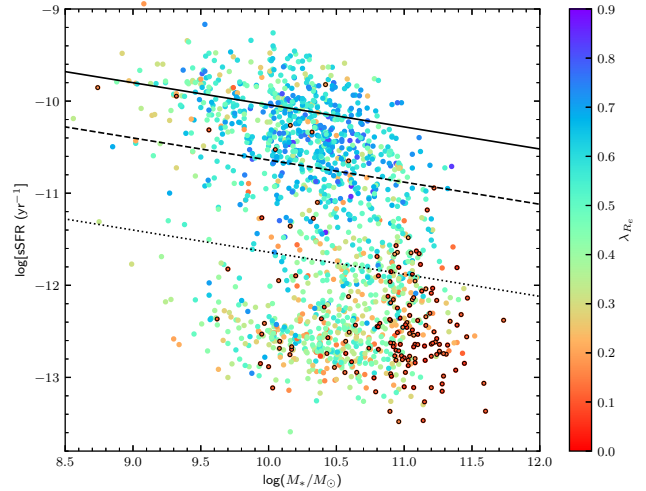

Figure 8. The distribution of SAMI galaxies with λ_{R_e} measurements in the sSFR-mass plane. Points are colour-coded by their λ_{R_e} value. Points with black edges are classified as slow rotators based the Cappellari (2016) definition. Diagonal lines indicate the location of the star formation main sequence from Renzini & Peng (2015) (solid line); 0.6 dex below the main sequence (dashed line); 1.6 dex below the main sequence (dotted line).

Comparing INT and SF galaxies we find $\Delta\lambda_{R_e}$ is between -0.03 and -0.21, while ΔC is $\simeq 0.1$–0.4. Averaged over all masses ($9.5 < \log(M_*/M_\odot) < 11.5$) the difference in λ_{R_e} between SF and INT galaxies is relatively small, with $\Delta\lambda_{R_e} = -0.081 \pm 0.011$, somewhat smaller than the eSp to S0 difference discussed above. The change in concentration between SF and INT galaxies, of $\Delta C = 0.309 \pm 0.026$, is also smaller than the eSp to S0 transition.

The difference between SF and PAS galaxies is much larger than that between SF and INT galaxies. The average (over $9.5 < \log(M_*/M_\odot) < 11.5$) difference is $\Delta\lambda_{R_e} = -0.187 \pm 0.009$, approximately 2.4 times larger than the difference between SF and INT galaxies. The concentration difference from SF to PAS galaxies is $\Delta C = 0.506 \pm 0.019$, 1.7 times larger than the difference between SF and INT galaxies.

4.4 Comparison of SAMI data to disc fading models

The changes that we see in the SAMI population can be directly compared to our disc fading models (see Figs 3 and 5). The mean SAMI values for eSp and S0 galaxies in the mass intervals above $\log(M_*/M_\odot) = 9.5$ (black points in Figs 3 and 5) lie along the simulated disc fading tracks (coloured points). The differences seen in the SAMI data are comparable to the disc fading models when we consider the most extreme model parameters. The evolution in the disc fading models is largest for $B/T = 0.5$. With 60° inclination, this leads to λ_{R_e} changing by -0.11 for 5 Gyr of disc fading. Only in the highest mass interval ($\log(M_*/M_\odot) > 11$) is the observed difference between eSp and S0 galaxies (-0.288 ± 0.044) too large for the most extreme disc fading models. Note that increasing the length of time that we fade the disc does not help very much, as most of the difference comes in the first few Gyr.

Our most extreme disc fading model ($B/T = 0.5$) gives a change in concentration of 0.13 for 5 Gyr of fading, compared to an observed change of 0.417 ± 0.026 for the median over all masses (a factor of 3.2 larger). Only the lowest mass interval, with $\Delta C = 0.175 \pm 0.088$, gives changes in concentration that are consistent with this most extreme disc fading model.

Table 4. The mean λ_R, concentration (R_{90}/R_{50}) and ellipticity (e) for SAMI galaxies separated by mass [in 0.5 bins of $\log(M_*/M_\odot)$] and SFR.

$\log(M_*/M_\odot)$	SF class	$\overline{\log(sSFR)}$ (yr^{-1})	N_g	$\overline{\lambda_R}$	$\overline{R_{90}/R_{50}}$	$\overline{e}$
9.5–10.0	SF	−10.06	118	0.542 ± 0.013	2.372 ± 0.026	0.408 ± 0.018
9.5–10.0	INT	−11.04	27	0.516 ± 0.031	2.472 ± 0.049	0.303 ± 0.036
9.5–10.0	PAS	−12.45	54	0.437 ± 0.018	2.644 ± 0.034	0.282 ± 0.023
10.0–10.5	SF	−10.21	328	0.591 ± 0.007	2.396 ± 0.017	0.399 ± 0.012
10.0–10.5	INT	−11.21	92	0.525 ± 0.017	2.590 ± 0.032	0.344 ± 0.020
10.0–10.5	PAS	−12.53	189	0.397 ± 0.010	2.841 ± 0.020	0.228 ± 0.011
10.5–11.0	SF	−10.44	134	0.580 ± 0.013	2.526 ± 0.030	0.371 ± 0.017
10.5–11.0	INT	−11.46	121	0.496 ± 0.014	2.827 ± 0.034	0.334 ± 0.018
10.5–11.0	PAS	−12.50	211	0.389 ± 0.009	3.044 ± 0.018	0.259 ± 0.010
11.0–11.5	SF	−10.75	12	0.644 ± 0.031	2.544 ± 0.096	0.376 ± 0.049
11.0–11.5	INT	−11.63	41	0.434 ± 0.024	2.946 ± 0.049	0.281 ± 0.028
11.0–11.5	PAS	−12.45	37	0.337 ± 0.022	3.147 ± 0.036	0.264 ± 0.022

Notes. Galaxies are separated into SFR classes (SF, intermediate, passive) based on their location with respect to the star-forming main sequence. The mean sSFR for each class is also listed, although we note that values below $\log(sSFR) \simeq -12.0$ are not reliable and should be regarded as non-detections. Only bins where the number of galaxies (N_g) is 5 or greater are given.
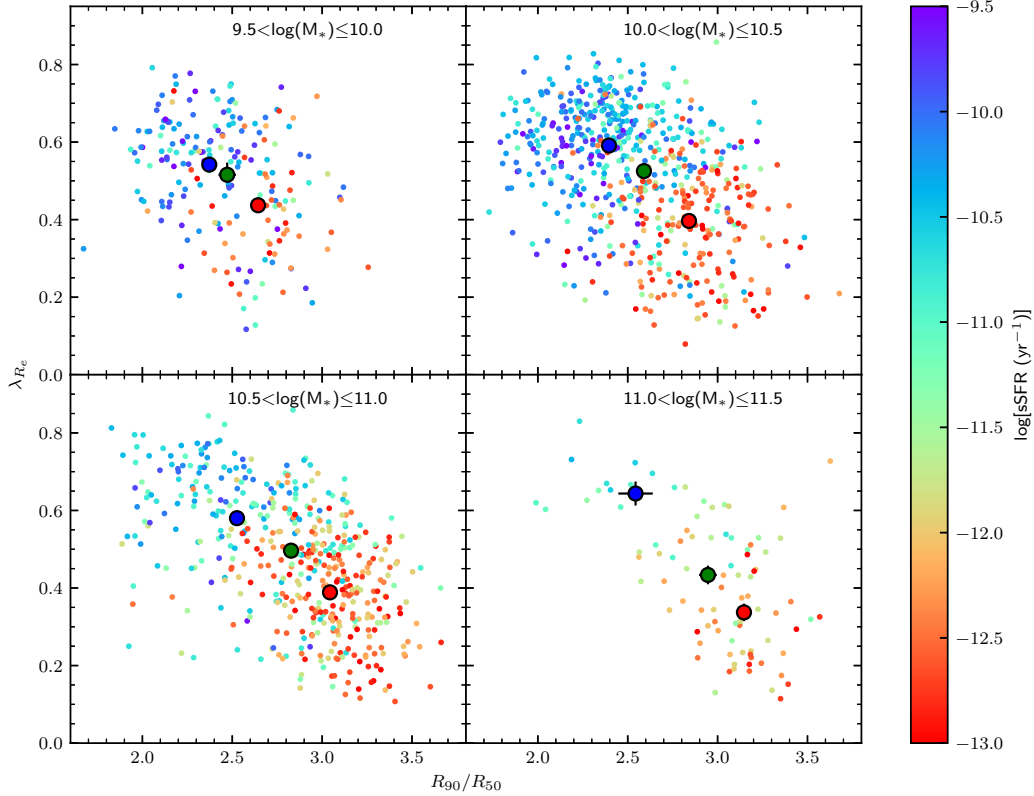
Figure 9. The distribution of our SAMI galaxies in the λ_R–concentration plane. Galaxies are separated into 0.5-dex intervals of stellar mass and then colour-coded by sSFR. The large points show the mean λ_R and concentration values for the SF (blue), INT (green), and PAS (red) galaxy samples that are defined based on their location with respect to the star-forming main sequence. The error bars on the large points show the error on the mean and are usually smaller than the points.

If we more realistically average over the range of possible disc fading models, then the overall impact of disc fading will be reduced. Assuming a flat distribution in B/T from 0 to 1, as well as a flat distribution of inclination, results in $\Delta\lambda_{R_e} = -0.055$ and $\Delta C = 0.082$. These values are not strongly sensitive to the range that we average over. If we average the models from $B/T = 0$ to 0.5 we find $\Delta\lambda_{R_e} = -0.057$ and $\Delta C = 0.085$. Comparing to

the measured values from SAMI (Table 3), we find that the disc fading is able to contribute ∼50 per cent of the difference seen between eSp and S0 galaxies in λ_{R_e}, but only $\simeq 20$ per cent of the difference in concentration. Therefore, while disc fading can make substantial contribution to the observed difference between eSp and S0 galaxies, it is not able to account for all of the difference.

We should also consider that the models we have constructed provide us with the most optimistic level of disc fading. That is, we have instantaneous quenching and a purely dispersion-supported bulge. If we take the *B/T* ratios that give us the largest change, we still fail to find sufficient disc fading. Further, the true *B/T* distribution of the population is broad (e.g. Morselli et al. 2017), particularly for early-type galaxies and early spirals. If all spirals can be transformed into S0s, those with lower bulge fraction (particularly late spirals) will not be so severely influenced by disc fading. Our model also assumes the bulge is older than the disc. Various works show that this may not always be the case (e.g. Fraser-McKelvie et al. 2018).

When we instead consider galaxies classed by their star formation properties we find a similar picture. Averaging over all mass (Table 3), our disc fading models can only contribute 30 per cent of the change in λ_{R_e} and 18 per cent of the change in concentration between galaxies close to the star-forming main sequence (our SF sample) and those that are fully passive (our PAS sample). Disc fading alone cannot change main-sequence galaxies to passive fast rotators.

The difference between galaxies in the main sequence (our SF sample) and those with some remaining star formation (our INT sample) is smaller than the difference with the PAS sample. In this case, disc fading can contribute 71 per cent of the change in λ_{R_e} and 30 per cent of the change in concentration.

The smaller difference between SF and INT galaxies is consistent with the picture discussed by Cortese et al. (2019). By comparing mass matched samples of central and satellite galaxies within the SAMI Galaxy Survey, they suggest that galaxies undergo little dynamical change until they are fully passive.

The impact of disc fading for kinematics will also be reduced if the bulges have some rotation. Decomposition of bulges shows that they have a range of dynamical properties. With a sample of spirals and S0s, Fabricius et al. (2012) find a diverse range of bulge kinematics, where bulges with higher Sérsic index have lower rotation. These objects are a mix of true and pseudo-bulges, with the pseudo-bulges having higher rotational support (although the two populations overlap). Méndez-Abreu et al. (2018) show that within a sample of S0 galaxies from the CALIFA Survey there is also a diversity of bulge rotational support. These results imply that the influence of disc fading we demonstrate is an upper limit.

The contribution of disc fading to the observed kinematic change comes from two sources. First is the larger photometric contribution to the bulge as the disc fades. However, there is a second contribution from the evolution of the measured effective radius of the galaxy. Given that the bulge has a smaller scale-length than the disc, the overall R_e will get smaller as the disc fades. As an example, we show in Fig. 10 the λ_R profile for $B/T = 0.5$ and inclination of 60°. The λ_R profile is shown for a model with $t_q = 0$ (black) and 5 Gyr (red), and R_e is marked by the vertical dotted line. In this case, the change in λ_R at a fixed radius is larger than the contribution due to changing R_e. This result is generally true for all models, but the exact contributions depend in detail on the model parameters.

The above argues that while disc fading can be a significant contribution to the change in the measured kinematics and concentration, it is not sufficient to match the differences seen in our data. Thus, other processes must also contribute significantly. These processes could include dynamical heating via interactions with other galaxies or the potential of the parent halo. However, another potential contribution could be from progenitor bias, which we will now discuss below.
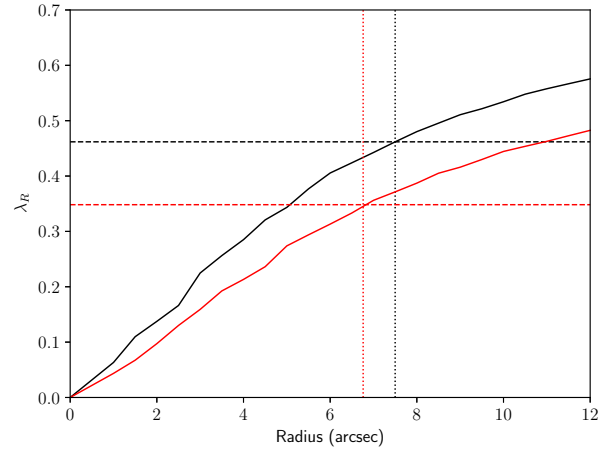

Figure 10. The λ_R profiles (solid lines) for a model galaxy with $B/T = 0.5$ and inclination of 60°, 0 Gyr (black), and 5 Gyr (red) after quenching. The vertical dotted lines indicate the value of R_e for each model, while the horizontal dashed lines show the values of λ_{R_e}.

4.5 The impact of progenitor bias

An important caveat on the work above is that we have assumed that the progenitors of present day S0s (or PAS) galaxies look like present day eSp (or SF) galaxies. As pointed out by Cortese et al. (2019) and others, this need not be the case. Thus, progenitor bias could also contribute to the observational differences that we see. In fact, observations of Hα emission suggest that in the past, galaxies had dynamically hotter discs (e.g. Wisnioski et al. 2015). In the local Universe, discs with younger stellar populations are thinner than those with older stars (e.g. van de Sande et al. 2018).

4.5.1 Progenitor bias from EAGLE simulations

Galaxies that continue to accrete gas (and therefore continue to form stars) will tend to spin-up with increasing cosmic time (e.g. Lagos et al. 2017). To quantitatively assess the impact of progenitor bias we take measurements of λ_{R_e} from the EAGLE simulations (Schaye et al. 2015; Lagos et al. 2017). We note that EAGLE size evolution (Furlong et al. 2017) is consistent with the observed size evolution found by van der Wel et al. (2014). As a result, this realistic size evolution will be implicitly included in the EAGLE λ_{R_e} measurement, given that they are made within one effective radius in the *r* band. We use the EAGLE reference model (Ref-L100N1504) and measure λ_{R_e} as described by Lagos et al. (2018) and make measurements at 13 redshift intervals between $z = 0$ and 1.8. Here and below we will only focus on measurements of λ_{R_e} (not concentration) as we are primarily concerned with the evolution of kinematics.

The galaxies in EAGLE are separated into passive and star forming, using a similar approach to the one we use with SAMI galaxies. This is also similar to the method used on EAGLE galaxies by Wright et al. (2019). We first define potential star-forming galaxies in EAGLE as those above log ($sSFR$/Gyr^{-1}) > $-2 + 0.5z$ following Furlong et al. (2015). Then, to define the star-forming main sequence for each redshift interval, we fit a linear relation to the median log (SFR) as a function of log (M_*). EAGLE galaxies within 0.6 dex of the best fitting main-sequence relation are defined as star forming. Those more than 1.6 dex below the main sequence are defined as passive.
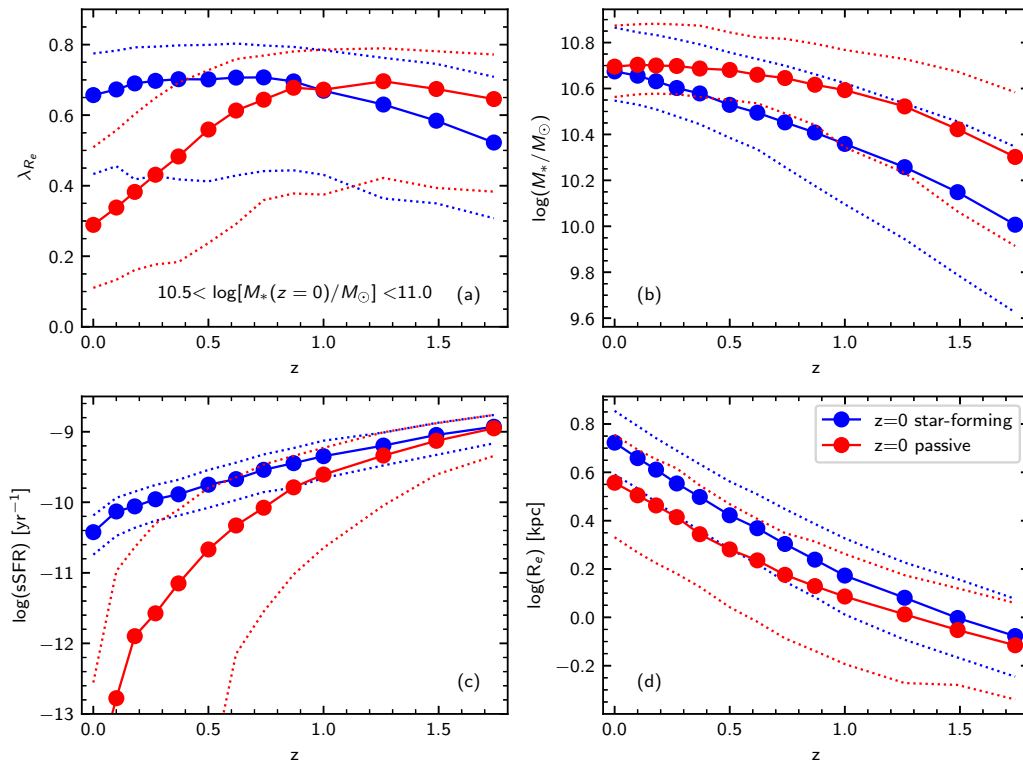
Figure 11. The median evolutionary tracks of galaxies selected from EAGLE to have $10.5 < \log (M_*/\mathrm{M}_\odot) \leq 11$ at $z = 0$. We separately show galaxies selected to be on the star-forming main sequence (blue points) and those that are passive (red points) at $z = 0$. Dotted lines in each panel show the 68th percentile range of values. We show the evolution for (panel a) λ_{R_e} (intrinsic edge-on), (panel b) stellar mass, (panel c) sSFR, and (panel d) r-band half-light radius.

Examples of the median EAGLE evolutionary tracks are shown in Fig. 11. Here we select EAGLE galaxies at $z = 0$ that have $\log (M_*/\mathrm{M}_\odot) = 10.5$–11 and are either star forming (blue points/lines) or passive (red points/lines) at $z = 0$. We then identify their progenitors at higher redshift and calculate the median values of λ_{R_e} (intrinsic edge-on value), stellar mass, sSFR, and r-band half-light radius. From high redshift, the λ_{R_e} of the $z = 0$ selected star-forming galaxies is increasing, but the evolution flattens below $z \sim 1$. In contrast, the passive galaxies decline in spin below $z < 1$. At $z > 1$, the progenitors of $z = 0$ passive galaxies have higher λ_{R_e} than star-forming galaxies. The reason for the offset in λ_{R_e} at high z can be explained by viewing the other panels in Fig. 11. Even though the progenitors of both the star-forming and passive galaxies have similar sSFRs above $z = 1$ (see Fig. 11c), they have different masses (Fig. 11b), as the mass growth of passive galaxies is slower at $z < 1$. As a result, the progenitors of the $z = 0$ star-forming and passive galaxies have different masses at high redshift, and we should not expect them to have the same λ_{R_e} or other quantities (such as size; see Fig. 11d), even if their sSFRs agree at an earlier epoch.

The difference in λ_{R_e} between star-forming and passive galaxies in EAGLE at $z = 0$ is large, at $\sim$0.25–0.35 (depending on stellar mass). This is similar to the difference we see in SAMI between passive and star-forming galaxies (see Table 3). The large difference between star-forming and passive galaxies in the EAGLE simulations is also several times larger than the difference that can be attributed to disc fading. The progenitors of the $z = 0$ passive galaxies in EAGLE are also seen to decline in λ_{R_e} by $\sim$0.3 between $z = 1$ and 0. This decline is several times larger than can be attributed to disc fading, so the EAGLE simulations do not support simple disc fading as the cause of the low λ_{R_e} in passive galaxies.

However, we note that the λ_{R_e} distributions in different simulation data sets can be quite different (van de Sande et al. 2019). Also, as is highlighted by Fig. 11, simply comparing the same mass galaxies at $z = 0$ is not a sufficiently robust test to examine the importance of disc fading, as the mass growth histories of passive and star-forming galaxies are different.

Using the EAGLE simulations, we now examine the progenitors of today's passive galaxies by looking at the value of λ_{R_e} for galaxies on the star-forming main sequence at different redshifts, but this time selected based on their stellar mass at redshift, z. We carry out this analysis in three stellar mass intervals, $10.0 < \log (M_*(z)/\mathrm{M}_\odot) \leq 10.5$, $10.5 < \log (M_*(z)/\mathrm{M}_\odot) \leq 11.0$, and $11.0 < \log (M_*(z)/\mathrm{M}_\odot) \leq 11.5$. In each case the masses correspond to the mass at the redshift where the properties are measured. These mass intervals allow us to be sure that we have sufficient galaxies per bin (at high mass) and are not impacted by resolution effects (at low mass). The λ_{R_e} values on the main sequence are shown in Fig. 12. We generate the measurements assuming that the galaxies are edge-on (Fig. 12a) and randomly inclined to the line of sight (Fig. 12b). For a given mass interval, $M_*(z)$, EAGLE galaxies on the main sequence have very similar median values of λ_{R_e} at all redshifts we examine. In fact, there is a small decline of up to $\sim$0.1 (for the highest mass interval) in λ_{R_e} from high to low redshift. We also note that for a given redshift, the value of λ_{R_e} on the main sequence is a function of mass. λ_{R_e} increases from $10.0 < \log (M_*(z)/\mathrm{M}_\odot) \leq 10.5$ (blue lines in Fig. 12) to $10.5 < \log (M_*(z)/\mathrm{M}_\odot) \leq 11.0$ (green lines). However, as we increase mass to $\log(M_*(z)/\mathrm{M}_\odot) > 11.0$, λ_{R_e} is lower again (red lines). This is consistent with the increased importance of mergers in mass growth at the highest stellar masses.

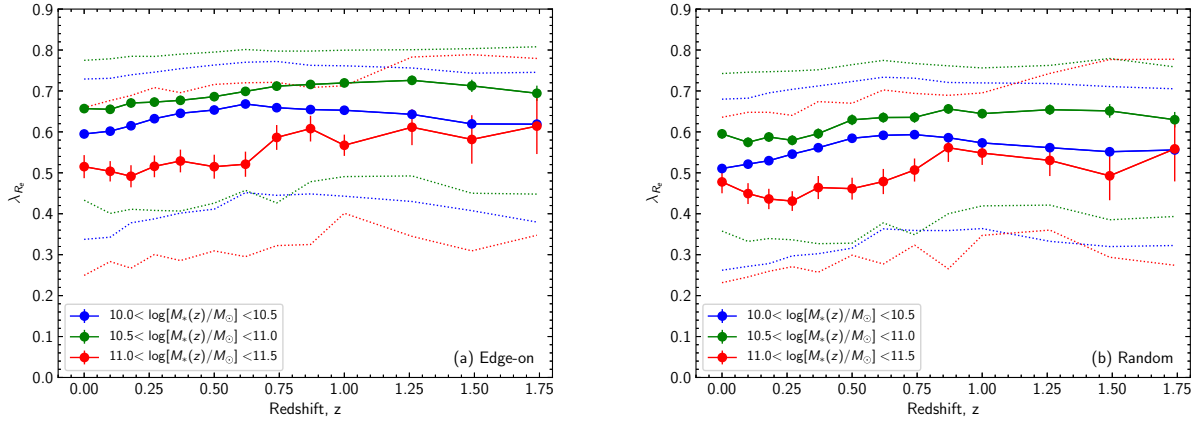**Figure 12.** The simulated λ_{R_e} for galaxies on the star-forming main sequence, based on measurements from EAGLE (Schaye et al. 2015; Lagos et al. 2017). Different colours correspond to stellar mass intervals, where the stellar mass is measured at each different epoch. Circles correspond to the median λ_{R_e}, the dotted lines show the 68th percentile range of values at the redshift of the measurement. In panel (a), we show results for the edge-on measurement of λ_{R_e}, while in panel (b), we use random inclinations. Error bars show the error on the median that is typically smaller than the points for all but the highest mass.
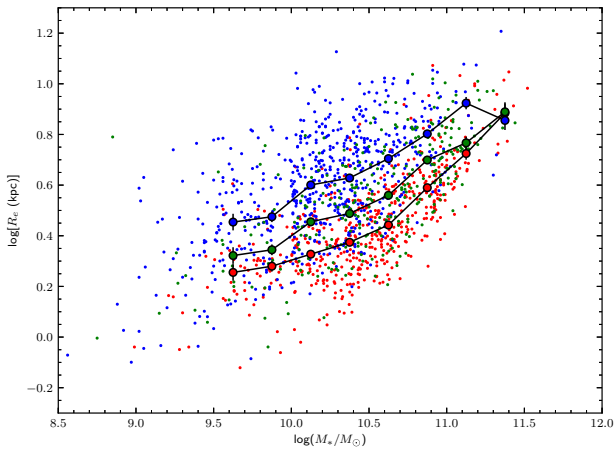
Figure 13. SAMI galaxies that we use in our analysis in the size (major axis R_e in SDSS r band) versus mass plane. Points are colour-coded based on their star formation classification as SF (blue), INT (green), or PAS (red). The large connected points with error bars denote the mean sizes in 0.25-dex stellar mass bins. We do not include slow rotators in this analysis.

4.5.2 Progenitor bias and size evolution

The known (e.g. van der Wel et al. 2014, and references therein) size evolution observed in the high redshift galaxy population also provides another source of progenitor bias. To quantify this we compare the size–mass relations for SAMI galaxies used in our analysis, separated into the SF, INT, and PAS populations (not including slow rotators; see Fig. 13). Here we are using the major axis R_e values estimated using MGE in the SDSS r band. There is a clear separation in size between SF and PAS galaxies that is largest at the low mass end. This is not surprising, given that the size–mass relation for early-type galaxies is known to be steeper than that of late types (e.g. Shen et al. 2003). The INT galaxies sit between the SF and PAS populations.

Taking a step further, we can use the ratio of mean size for SF and PAS or INT galaxies to quantify how much size difference there is between the populations. These ratios are shown in Fig. 14(a). At stellar masses below $\log(M_*/M_\odot) < 10.5$ the size ratio is relatively constant, while at higher masses (grey shaded region) it declines.
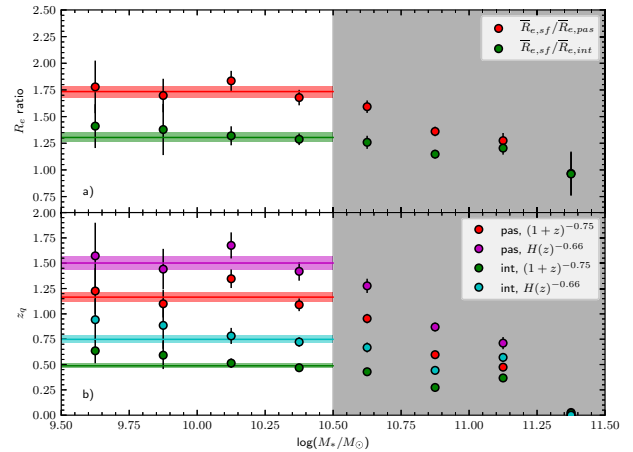

Figure 14. Panel (a): the ratio of mean size as a function of stellar mass for SAMI galaxies used in our analysis. Red points denote $R_{e, SF}/R_{e, PAS}$ and green points denote $R_{e, SF}/R_{e, INT}$. Panel (b): the inferred quenching redshift, z_q, for PAS and int galaxies based on their size ratios compared to SF galaxies. We estimate z_q using two different fitted forms for size evolution from van der Wel et al. (2014) where the evolution is either a function of $(1 + z)$ or $H(z)$. The grey shaded region indicates the mass range where mergers dominate mass growth, so we do not consider these points. Horizontal lines are the average (over stellar masses $\log(M_*/M_\odot) < 10.5$) z_q for each sample and assumed evolution.

Several authors (e.g. Robotham et al. 2014) have pointed out that at masses greater than $\sim M^*$, galaxy build-up is dominated by merging, while at lower masses *in situ* star formation dominates. Given that locally $\log(M^*/M_\odot) \simeq 10.66$ (Baldry et al. 2012), we will only consider size information below $\log(M^*/M_\odot) = 10.5$. The average size ratio for $R_{e, SF}/R_{e, PAS}$ is 1.75 ± 0.05 (red horizontal line in Fig. 14), while for $R_{e, SF}/R_{e, INT}$, it is 1.30 ± 0.04 (green horizontal line in Fig. 14). In comparison to these values, the change in size inferred by our disc fading models is only 10 per cent at most (with $B/T = 0.5$; see Fig. 4). This strongly rules out the simple proposition that the progenitors of today's passive galaxies are the same as today's star-forming galaxies. The intermediate galaxies are also inconsistent with this proposition. These size differences mean that progenitor bias must play an important role.

4.5.3 Using size evolution to infer quenching time

Estimates of size evolution have previously been published by a number of authors including van der Wel et al. (2014). They find that for star-forming galaxies the zero-point evolution of the size–mass relation can be fit as either $\sim(1+z)^{-0.75}$ or $\sim H(z)^{-0.66}$, where $H(z)$ is the Hubble parameter at redshift z. If we make the simplifying assumption that no further structural change occurs after a galaxy starts to leave the star-forming main sequence, then the size evolution model can be used to infer the redshift at which the galaxy quenched (which we will call z_q). For example, the value of z_q for the PAS population assuming evolution parameterized by $(1+z)$, we find

$$z_q = (1+z_{\rm obs}) \left(\frac{\overline{R}_{\rm e,SF}}{\overline{R}_{\rm e,PAS}} \right)^{1/0.75} - 1, \qquad (12)$$

where $z_{\rm obs}$ is the redshift at which the SAMI galaxies are observed. What we are effectively doing here is to use the fitted evolutionary trends from van der Wel et al. (2014) to find the redshift at which star-forming main-sequence galaxies had the same size as the PAS or INT galaxies within the SAMI sample.

In the above, we are assuming that there is no further size evolution (other than due to disc fading) once disc galaxies have quenched. However, observationally we know that size evolution of the passive population is stronger than for the star-forming population. This strong evolution of the passive population is partly driven by a real decline in the density of compact galaxies as we move to the present day (van der Wel et al. 2014), particular at high mass ($>5 \times 10^{10}\,{\rm M}_\odot$). At lower mass, it is plausible that most of the size evolution of the passive population is driven by the addition of larger star-forming disc galaxies as they quench. As a result, it does not make sense to incorporate the measured size evolution of the passive population into our model. We note that invariably the estimate of z_q based on size is only approximate. We are not aiming to construct a detailed model that takes into account all potential elements of size evolution.

In summary the steps we take to estimate z_q from size evolution are as follows:

(i) Find the size ratio between the observed SF and PAS (or INT) SAMI galaxy populations for each mass interval (see Fig. 14a).

(ii) Assume there is no intrinsic dynamical evolution in a galaxy following its quenching and that size evolution due to disc fading is not significant.

(iii) Use fits to the observed size evolution (van der Wel et al. 2014) to infer the redshift at which quenching takes place (see equation 12 and Fig. 14b).

The results of our z_q calculation can be seen in Fig. 14(b) and here we again only consider galaxies at $\log(M_*/{\rm M}_\odot) < 10.5$. For PAS galaxies the inferred mean z_q is 1.18 ± 0.05 and 1.53 ± 0.07 (for the $(1+z)$ and $H(z)$ evolution parametrizations, respectively). The difference between the $(1+z)$ and $H(z)$ evolution estimates of z_q is because the models diverge somewhat at $z = 0$ (see fig. 6 of van der Wel et al. 2014). Other estimates of size evolution, including a constraint at $z \simeq 0$ from SDSS find a solution that is closer to the $H(z)$ model (Trujillo et al. 2006); however, for completeness, we consider both parametrizations. For INT galaxies, the z_q values are 0.48 ± 0.02 and 0.74 ± 0.04. The mean values below $\log(M_*/{\rm M}_\odot) = 10.5$ are indicated in Fig. 14(b) by the horizontal lines. It is clear from these values and Fig. 14(b) that uncertainties in the evolutionary model contribute significantly to the calculated z_q. Residual size evolution (e.g. due to disc fading; see Fig. 4) could also contribute to uncertainty on z_q, but as we discuss above, this is small compared to the overall evolution in size seen in the galaxy population.

4.5.4 Combining disc fading and progenitor bias

Carollo et al. (2016) demonstrated from photometric measurements that the differences in B/T between quenched and star-forming satellite galaxies can be largely attributed to disc-fading. However, Carollo et al. also show that the size difference between quenched and star-forming galaxies is too large to be caused by disc fading. This is consistent with our measurements, that also consider dynamics.

The morphological mix of galaxies in groups is known to evolve strongly, with an increase in the fraction of S0s by approximately a factor of 2 since $z \simeq 0.5$ (Just et al. 2010). If we assume there is little mass growth in passive discs once they are quenched (see Figs 11b and c), then the value of $\lambda_{R_e}(z)$ for main-sequence galaxies in Fig. 12 provides us an estimate of their progenitors' spin at the point that they quench. If we conservatively say that most S0s have transformed from star-forming discs since $z \sim 1$, then the EAGLE simulation results suggest that their progenitors had λ_{R_e} that is slightly higher than current star-forming discs of the same mass. For example, the difference $\lambda_{R_e}(z=0) - \lambda_{R_e}(z=1) = -0.06, -0.05$, and -0.07 for EAGLE main-sequence galaxies in mass intervals $\log(M_*/{\rm M}_\odot) = 10–10.5, 10.5–11.0$, and $11.0–11.5$, respectively. These values are similar to the change expected from 5 Gyr of our disc fading models ($\Delta\lambda_{R_e} = -0.055$, averaged over all B/T and inclination). As a result, disc fading is only sufficient to evolve galaxies from their typical λ_{R_e} on the main sequence at $z = 1$ to the typical value of λ_{R_e} on the main sequence at $z = 0$. This is not a sufficient change to evolve galaxies on the main sequence to $z = 1$ to the observed λ_{R_e} of passive galaxies at $z = 0$.

We can also use our estimates of z_q from size evolution to obtain another prediction of the amount of progenitor bias in λ_{R_e}. For PAS galaxies, $z_q = 1.13–1.47$ (depending on the evolutionary model used). At the high end of this redshift range, the λ_{R_e} of galaxies on the main sequence (Fig. 12) starts to decline towards higher redshift; however, this decline is small. As a result, for all three mass intervals shown in Fig. 12, λ_{R_e} in the main sequence is higher at $z_q = 1.13–1.47$ than it is at $z = 0$.

We consider our size evolution estimates of quenching time to be reasonable at $\log(M_*/{\rm M}_\odot) = 10–10.5$ (Section 4.5.3 and Fig. 14). In this mass range, the λ_{R_e} on the main sequence is between 0.06 ($z_q = 1.13$) and 0.04 ($z_q = 1.47$) higher than at $z = 0$. The observed difference between $z = 0$ PAS and SF galaxies in this mass range is -0.194 ± 0.012. If we add the progenitor bias to this, then the range for the total change in spin is between -0.234 and -0.254, where the size of the allowable range is dominated by the uncertainty on the estimated quenching time, not the uncertainty in observed λ_{R_e} values. In contrast, the change allowable due to disc fading (averaging over all B/T) is -0.057. Disc fading appears to only contribute a small fraction of the required change, meaning that intrinsic dynamical evolution (i.e. changes in the orbital distribution of stars) must be an important contributing factor. It is also worth noting that our disc fading models are likely to be optimistic in the amount of apparent kinematic change they cause. We assume a purely dispersion-supported bulge (no rotation) and a 10 Gyr old bulge stellar population. A bulge with some rotation, or younger stars will reduce the impact of disc fading.

The galaxies from the EAGLE simulation on the SF main sequence at $\log(M_*/{\rm M}_\odot) > 11$ have the largest increase in λ_{R_e} as redshift increases. These galaxies also show the largest observational difference in λ_{R_e} between SF and PAS (or eSp and S0s). In this case, it is even more clear that intrinsic dynamical evolution must play the main role in transforming galaxies. At high masses mergers are more important than *in situ* star formation for mass growth

(e.g. Robotham et al. 2014). Therefore, we expect that many of the passive fast rotators at $\log(M_*/M_\odot) > 11$ may be built up from mergers. These mergers will need to have impact parameters and total angular momentum such that after the merger, they still have significant rotation. Lagos et al. (2018) used EAGLE simulations to show that galaxy mergers consistently decrease λ_{R_e} unless they are very gas-rich. Minor mergers with gas fraction <0.1 can reduce λ_{R_e} by 20–40 per cent on average, while major mergers of the same gas fractions reduce λ_{R_e} by 50 per cent (see fig. 14 of Lagos et al. 2018). Hence, the decrease in λ_{R_e}, even of main-sequence galaxies, is consistent with mergers affecting them systematically at $z < 1$.

To confirm the contribution of progenitor bias, we will need to make stellar kinematic observations at higher redshift. Some work in this area has already been done using the LEGA-C survey (Bezanson et al. 2018). LEGA-C finds that V/σ for passive galaxies is reduced from $z = 0.8$ to 0, suggesting some spin-down of massive passive galaxies. However, the exact amount of spin-down is still uncertain (e.g. see discussion in the appendix of Bezanson et al. 2018). These measurements are also seeing-convolved estimates of V/σ evolution and seeing corrections are dependent on both V/σ and size (Harborne et al. 2020a), so the intrinsic evolution is harder to discern.

5 CONCLUSIONS

We use dynamically self-consistent models to estimate the signature of disc fading on the observed kinematics and structural properties of galaxies. In particular, we assess how the changing contribution from bulge and disc can influence galaxy properties, despite no change in the mass fraction in each component. Specifically we conclude as follows:

(i) In galaxies with an old bulge and a star-forming disc, quenching the disc leads to a reduction in measured spin, λ_{R_e}, and an increase in measured concentration. These trends are due to the reduction in the light weighted contribution of the disc. Unsurprisingly, this is most significant for systems where the mass of the bulge and disc are relatively equal. For $B/T = 0.5$, we find that 5 Gyr of quenching leads to a reduction of 0.12 in λ_{R_e}. At the same time, the measured r-band concentration increases by 0.13. Averaged over all B/T we find 5 Gyr of disc fading leads to change in λ_{R_e} of -0.055 and a change in concentration of 0.082.

(ii) We measure the difference in λ_{R_e} and concentration between early spirals (classified eSp) and S0s from the SAMI Galaxy Survey. We find S0s have an average λ_{R_e} that is smaller than eSp galaxies, with the mean $\Delta\lambda_{R_e} = -0.132 \pm 0.013$. The mean difference in concentration is $\Delta C = 0.417 \pm 0.026$. This difference is in the same qualitative sense as our disc fading models but somewhat larger in amplitude, only becoming comparable when using the most extreme models ($B/T = 0.5$).

(iii) When we separate SAMI galaxies by their SFR relative to the main sequence (instead of morphology), we find that the difference between regular star-forming galaxies (on the main sequence) and passive galaxies (>1.6 dex below the main sequence) is too great to be due to disc fading alone.

(iv) The difference in spin and concentration between main-sequence galaxies and those with weak star formation (0.6–1.6 dex below the main sequence) is less than for passive galaxies.

(v) Size evolution plays an important role in progenitor bias, but as a result can be used as a tool to estimate the time at which galaxies quenched and left the main sequence (under a number of assumptions).

(vi) We use the EAGLE simulations to estimate the amount of progenitor bias that can contribute to λ_{R_e} differences. For a fixed mass range at redshift z, the spin of main-sequence galaxies increases slightly from $z = 0$ until at least $z = 1$ (dependent on mass). This progenitor bias does not help to bring disc fading models into agreement with the data, as it goes in the opposite sense to that required. We conclude that disc fading is not sufficient to explain the λ_{R_e} difference between star-forming and passive (or eSp and S0) galaxies at $z = 0$. Instead, intrinsic evolution of the stellar dynamics of the galaxies must dominate.

The progenitors of today's S0s are in most cases likely to be spiral galaxies at an earlier epoch (e.g. Dressler et al. 1997; Just et al. 2010). Spatially resolved spectroscopic surveys capable of measuring the stellar kinematics in discs should be able to quantify the importance of evolving stellar disc dispersion. Sampling a redshift range $z = 0.25$–0.50 would be sufficient to study 3–5 Gyr of evolution. Such observations are now becoming possible with medium-deep surveys covering large areas using instruments such as the Multi Unit Spectroscopic Explorer (MUSE; Bacon et al. 2010). One such project is the Middle-Ages Galaxy Properties with Integral Field Spectroscopy (MAGPI; Foster et al. 2020) survey currently proceeding on the Very Large Telescope with MUSE.

Future work should also examine whether the kinematic and structural properties of S0 galaxies are dependent on the environment. If dynamical effects contribute to the formation process of S0s, differences in interactions as a function of environment could lead to measurable environmental trends.

DATA AVAILABILITY

The SAMI data used in this paper, including kinematic measurements, are included in SAMI Data Release 3 (Croom et al. 2021) available via Australian Astronomical Optics' Data Central, https://datacentral.org.au/. Simulation results for all models are available online as part of this publication.

REFERENCES

AAO Software Team, 2015, Astrophysics Source Code Library, record ascl:1505.015

Abazajian K. N. et al., 2009, ApJS, 182, 543

Ahn C. P. et al., 2012, ApJS, 203, 21

Allen J. T. et al., 2014, Astrophysics Source Code Library, record ascl:1407.006

Allen J. T. et al., 2015, MNRAS, 446, 1567

Bacon R. et al., 2010, in McLean I. S., Ramsay S. K., Takami H., eds, Proc. SPIE Conf. Ser. Vol. 7735, Ground-based and Airborne Instrumentation for Astronomy III. SPIE, Bellingham. p. 773508

Baldry I. K. et al., 2012, MNRAS, 421, 621

Baldwin J. A., Phillips M. M., Terlevich R., 1981, PASP, 93, 5

Beeston R. A. et al., 2018, MNRAS, 479, 1077

Bekki K., 1998, ApJ, 502, L133

Bekki K., Couch W. J., 2011, MNRAS, 415, 1783 (BC11)

Bezanson R. et al., 2018, ApJ, 858, 60

Bland-Hawthorn J. et al., 2011, Opt. Express, 19, 2649

Brough S. et al., 2017, ApJ, 844, 59

Bryant J. J. et al., 2015, MNRAS, 447, 2857

Bryant J. J., Bland-Hawthorn J., Fogarty L. M. R., Lawrence J. S., Croom S. M., 2014, MNRAS, 438, 869

Bundy K. et al., 2015, ApJ, 798, 7

Butcher H., Oemler A., Jr, 1984, ApJ, 285, 426

Cappellari M. et al., 2007, MNRAS, 379, 418

Cappellari M. et al., 2013, MNRAS, 432, 1709

Cappellari M., 2002, MNRAS, 333, 400

Cappellari M., 2016, ARA&A, 54, 597

Cappellari M., Emsellem E., 2004, PASP, 116, 138

Carollo C. M. et al., 2016, ApJ, 818, 180

Cen R., 2014, ApJ, 781, 38

Chabrier G., 2003, PASP, 115, 763

Christlein D., Zabludoff A. I., 2004, ApJ, 616, 192

Cortese L. et al., 2016, MNRAS, 463, 170

Cortese L. et al., 2019, MNRAS, 485, 2656

Cortese L., Boselli A., Franzetti P., Decarli R., Gavazzi G., Boissier S., Buat V., 2008, MNRAS, 386, 1157

Cortesi A. et al., 2013, MNRAS, 432, 1010

Croom S. M. et al., 2012, MNRAS, 421, 872

Croom S. M. et al., 2021, MNRAS, preprint (arXiv:2101.12224)

D'Eugenio F. et al., 2021, MNRAS, 504, 5098

Davies L. J. M. et al., 2019, MNRAS, 483, 1881

de Grijs R., 1998, MNRAS, 299, 595

de Vaucouleurs G., 1948, Ann. Astrophys., 11, 247

Dressler A. et al., 1997, ApJ, 490, 577

Dressler A., 1980, ApJ, 236, 351

Driver S. P. et al., 2011, MNRAS, 413, 971

Elbaz D. et al., 2007, A&A, 468, 33

Emsellem E. et al., 2007, MNRAS, 379, 401

Emsellem E. et al., 2011, MNRAS, 414, 888

Emsellem E., Monnet G., Bacon R., 1994, A&A, 285, 723

Fabricius M. H., Saglia R. P., Fisher D. B., Drory N., Bender R., Hopp U., 2012, ApJ, 754, 67

Fathi K., Allen M., Boch T., Hatziminaoglou E., Peletier R. F., 2010, MNRAS, 406, 1595

Fogarty L. M. R. et al., 2015, MNRAS, 454, 2050

Foster C. et al., 2020, PASA , preprint (arXiv:2011.13567)

Fraser-McKelvie A., Aragón-Salamanca A., Merrifield M., Tabor M., Bernardi M., Drory N., Parikh T., Argudo-Fernández M., 2018, MNRAS, 481, 5580

Furlong M. et al., 2015, MNRAS, 450, 4486

Furlong M. et al., 2017, MNRAS, 465, 722

Gadotti D. A., Baes M., Falony S., 2010, MNRAS, 403, 2053

Graham M. T. et al., 2018, MNRAS, 477, 4711

Gunn J. E., Gott J. R. III, 1972, ApJ, 176, 1

Harborne K. E., Power C., Robotham A. S. G., Cortese L., Taranu D. S., 2019, MNRAS, 483, 249

Harborne K. E., van de Sande J., Cortese L., Power C., Robotham A. S. G., Lagos C. D. P., Croom S., 2020a, MNRAS, 497, 2018

Harborne K. E., Power C., Robotham A. S. G., 2020b, Publ. Astron. Soc. Aust., 37, e016

Head J. T. C. G., Lucey J. R., Hudson M. J., Smith R. J., 2014, MNRAS, 440, 1690

Johnston E. J., Aragón-Salamanca A., Merrifield M. R., 2014, MNRAS, 441, 333

Just D. W., Zaritsky D., Sand D. J., Desai V., Rudnick G., 2010, ApJ, 711, 192

Kauffmann G. et al., 2003, MNRAS, 346, 1055

Kennicutt Robert C. J., Tamblyn P., Congdon C. E., 1994, ApJ, 435, 22

Koopmann R. A., Kenney J. D. P., 2004, ApJ, 613, 866

Kuijken K. et al., 2019, A&A, 625, A2

Kuijken K., Dubinski J., 1995, MNRAS, 277, 1341

Lagos C. D. P., Theuns T., Stevens A. R. H., Cortese L., Padilla N. D., Davis T. A., Contreras S., Croton D., 2017, MNRAS, 464, 3850

Lagos C. D. P., Schaye J., Bahé Y., Van de Sande J., Kay S. T., Barnes D., Davis T. A., Dalla Vecchia C., 2018, MNRAS, 476, 4327

Lange R. et al., 2016, MNRAS, 462, 1470

Larson R. B., Tinsley B. M., Caldwell C. N., 1980, ApJ, 237, 692

Lewis I. et al., 2002, MNRAS, 334, 673

Maraston C., Strömbäck G., 2011, MNRAS, 418, 2785

Masters K. L. et al., 2010, MNRAS, 405, 783

Mathieu A., Merrifield M. R., Kuijken K., 2002, MNRAS, 330, 251

Medling A. M. et al., 2018, MNRAS, 475, 5194

Méndez-Abreu J. et al., 2018, MNRAS, 474, 1307

Moffat A. F. J., 1969, A&A, 3, 455

Morselli L., Popesso P., Erfanianfar G., Concas A., 2017, A&A, 597, A97

Navarro J. F., Frenk C. S., White S. D. M., 1997, ApJ, 490, 493 (NFW)

Nulsen P. E. J., 1982, MNRAS, 198, 1007

Oh S. et al., 2020, MNRAS, 495, 4638

Owers M. S. et al., 2017, MNRAS, 468, 1824

Pak M., Lee J. H., Jeong H., Kim S., Smith R., Lee H.-R., 2019, ApJ, 880, 149

Pastrav B. A., Popescu C. C., Tuffs R. J., Sansom A. E., 2013, A&A, 557, A137

Peletier R. F., Valentijn E. A., Moorwood A. F. M., Freudling W., 1994, A&AS, 108, 621

Pillepich A. et al., 2019, MNRAS, 490, 3196

Querejeta M. et al., 2015, A&A, 579, L2

Ramos-Martínez M., Gómez G. C., Pérez-Villegas Á., 2018, MNRAS, 476, 3781

Rawle T. D., Lucey J. R., Smith R. J., Head J. T. C. G., 2013, MNRAS, 433, 2667

Renzini A., Peng Y.-J., 2015, ApJ, 801, L29

Robotham A. S. G. et al., 2014, MNRAS, 444, 3986

Roediger E., Brüggen M., 2007, MNRAS, 380, 1399

Roediger E., Brüggen M., 2008, MNRAS, 388, L89

Sánchez S. F. et al., 2016, A&A, 594, A36

Sánchez-Blázquez P. et al., 2006, MNRAS, 371, 703

Schaefer A. L. et al., 2017, MNRAS, 464, 121

Schaefer A. L. et al., 2019, MNRAS, 483, 2851

Schawinski K. et al., 2009, MNRAS, 396, 818

Schaye J. et al., 2015, MNRAS, 446, 521

Scott N. et al., 2009, MNRAS, 398, 1835

Scott N. et al., 2018, MNRAS, 481, 2299

Sérsic J. L., 1963, Bol. Asoc. Astron. La Plata Argentina, 6, 41

Shanks T. et al., 2015, MNRAS, 451, 4238

Sharp R. et al., 2006, in McLean I. S., Iye M., eds, Proc. SPIE Conf. Ser. Vol. 6269, Ground-based and Airborne Instrumentation for Astronomy. SPIE, Bellingham, p. 62690G

Sharp R. et al., 2015, MNRAS, 446, 1551

Shen S., Mo H. J., White S. D. M., Blanton M. R., Kauffmann G., Voges W., Brinkmann J., Csabai I., 2003, MNRAS, 343, 978

Smith M. W. L. et al., 2012, ApJ, 748, 123

Strateva I. et al., 2001, AJ, 122, 1861

Tapia T., Eliche-Moral M. C., Aceves H., Rodríguez-Pérez C., Borlaff A., Querejeta M., 2017, A&A, 604, A105

Taranu D. S. et al., 2017, ApJ, 850, 70

Taranu D. S., Dubinski J., Yee H. K. C., 2013, ApJ, 778, 61

Tiley A. L. et al., 2019, MNRAS, 482, 2166

Trujillo I. et al., 2006, ApJ, 650, 18

van de Sande J. et al., 2017a, MNRAS, 472, 1272

van de Sande J. et al., 2017b, ApJ, 835, 104

van de Sande J. et al., 2018, Nat. Astron., 2, 483

van de Sande J. et al., 2019, MNRAS, 484, 869

van der Wel A. et al., 2014, ApJ, 788, 28

Vijayaraghavan R., Sarazin C., 2017a, ApJ, 841, 22

Vijayaraghavan R., Sarazin C., 2017b, ApJ, 848, 63

Widrow L. M., Pym B., Dubinski J., 2008, ApJ, 679, 1239

Williams M. J., Bureau M., Cappellari M., 2010, MNRAS, 409, 1330

Wisnioski E. et al., 2015, ApJ, 799, 209

Wright R. J., Lagos C. D. P., Davies L. J. M., Power C., Trayford J. W., Wong O. I., 2019, MNRAS, 487, 3740

SUPPORTING INFORMATION

Supplementary data are available at *MNRAS* online.

suppl_data

Please note: Oxford University Press is not responsible for the content or functionality of any supporting materials supplied by the authors. Any queries (other than missing material) should be directed to the corresponding author for the article.

This paper has been typeset from a TEX/LATEX file prepared by the author.